J Ther Eng, Vol. 11, No. 2, pp. 577−602, March, 2025

Journal of Thermal Engineering
Web page info: https://jten.yildiz.edu.tr
DOI: 10.14744/thermal.0000933

Research Article

Hydrothermal investigation of a nanofluid flow in a compound microchannels

Sarab Salih SHEKHO[1], Ahmed Fouad AL-NEAMA[1,*]

[1]*Department of Mechanical Engineering, University of Mosul, College of Engineering, 41002, Mosul, Iraq*

ARTICLE INFO

Article history
Received: 10 February 2024
Revised: 29 April 2024
Accepted: 13 May 2024

Keywords:
Al_2O_3; Compound MCHSs; CuO; Nanofluid; Reentrant Microchannels

ABSTRACT

In this research, CFD modelling was employed to quantitatively investigate the influence of laminar forced convective heat transfer employing Al_2O_3/water and CuO/water nanofluids as working mediums, with a volume concentration (φ) of 4%, in three distinct compound microchannel heat sinks (MCHSs). Each MCHS features a bottom circular cavity and a narrow slot (namely rectangular, trapezoidal, or semicircular reentrant) attached to the circular cavity's crest. Their cooling efficacy was compared to that of a traditional straight rectangular MCHS. Both nanoparticles had a diameter of 47nm, and the nanofluid's thermophysical properties were temperature-dependent. The fluid inlet temperature was maintained at 20°C, whereas the volumetric flow rate (Q_{in}) ranged from 20 to 100ml/min. The results demonstrated that employing a hybrid heat transfer augmentation technique with CuO/water nanofluid at Q_{in}=100ml/min increased the average Nusselt number (Nu_{avg}) of the rectangular reentrant MCHS by 7.1% and decreased the total thermal resistance (R_{th}) of the semicircular reentrant MCHS by 16.8%, compared to using water in a traditional MCHS. However, this improvement in Nu_{avg} was accompanied by a 45.8% increment in the total pressure drop (ΔP_t) when the rectangular reentrant MCHS within CuO/water nanofluid was used instead of the traditional MCHS with pure water. This improved heat transfer is attributed to flow separation, fluid acceleration in the main flow, and intensified fluid mixing in the three newly proposed MCHSs.

Cite this article as: Shekho SS, Al-Neama AF. Hydrothermal investigation of a nanofluid flow in a compound microchannels. J Ther Eng 2025;11(2):577−602.

INTRODUCTION

Micro-scale heat transfer devices are now indispensable tools in a wide range of common applications, including integrated circuits (IC), computer chips, and biomedical applications [1]. Hence, microfluidic-cooling heat sinks have been employed to tackle the rigorous thermal management issues in many high-power applications. The concept of MCHS cooling was first proposed by Tuckerman and Pease [2]. In the aftermath of this outstanding work, various MCHS materials were utilized, and channel dimensions have been thoroughly examined with the purpose of improving heat transfer.

Generally, the majority of the researchers observed that straight microchannels have performance limitations and

*Corresponding author.
*E-mail address: ahmedfalneama@uomosul.edu.iq, ahmedfalneama@gmail.com

This paper was recommended for publication in revised form by Editor-in-Chief Ahmet Selim Dalkılıç

Published by Yıldız Technical University Press, İstanbul, Turkey

the disadvantage of being unable to eliminate the high heat flux produced by ultra-high-performance electronic devices due to the thermal boundary layer thickness (δ_{th}) development along the microchannel walls, hindering efficient heat transfer. Thus, many approaches have been developed in the quest to improve MCHS overall performance with minimal thermal resistance (R_{th}) and pressure drop (ΔP). There are two main kinds of heat removal augmentation techniques: active and passive. In contrast to the passive approach, the active technique involves utilizing extrinsic power in the system to augment heat transfer performance. The passive technique was commonly favoured over the active approach because of its more affordable price and lack of mechanical moving parts. As a result, numerous novel passive techniques for replacing the straight channel have been proposed [3].

Passive surface modifications can induce flow disruption; recently, zigzag [4], wavy or corrugated [5, 6], serpentine [7–10], spiral [11], interrupted [12], reentrant-shaped microchannels [13–16], ribs [17–22], cavities or groove structures [23, 24], and offset strip fins [25–27] have been suggested as flow channel modification strategies for promoting flow instabilities and improving microchannel forced convection performance. These strategies encourage the main stream to split at the leading edge, which causes the boundary layer to be reinitialized, greater mixing, and an increase in flow disruptions as well as velocity gradients close to the heated wall, resulting in higher heat transport.

Dai et al. [4] and Parlak [5] explored numerically the hydrothermal characteristics of zigzag and wavy MCHS configurations and compared them to the straight one. They noticed that the averaged Nusselt number (Nu_{avg}) for the wavy microchannel design was 10% greater than that of the zigzag microchannel and 40% greater than that of the straight microchannel. A wavy microchannel has a ΔP that is nearly equal to that of a zigzag microchannel model and 10kPa higher than that of a straight rectangular MCHS. Lin et al. [6] examined numerically the hydrodynamic and thermal characteristics, as well as the impact of the aspect ratio on the wavy microchannel with individual wavelength and amplitude variations along the direction of the working fluid flow. They found that when the wavelength decreases or wave amplitude increases between two adjacent wavy units along the flow direction, the R_{th} value and temperature disparity on the heat flux bottom surface are less than that of a traditional microchannel. They noticed the same manner when the aspect ratio was reduced. Al-Neama et al. [7] examined the benefits of three different configurations of serpentine MCHS designs using complementary experimental and numerical methods with single, double, and three path serpentine configurations. A comparison of their performance was conducted with a design based on conventional straight rectangular MCHS in terms of R_{th}, ΔP, and Nu_{avg}. According to the findings, serpentine channel curves play a significant role in enhancing heat transport by inhibiting the thickness of both the hydrodynamic (δ_{hy}) and thermal (δ_{th}) boundary layers from attempting to reach a fully developed condition.

A numerical and experimental investigation was performed by Deng et al. [13] to explore the forced convective heat transfer of single-phase laminar flow on an innovative Ω-shaped reentrant copper MCHS. This new design outperformed traditional MCHS in terms of improving heat transfer due to flow separation and fluid mixing induced by throttling effects. To boost fluid mixing and disturb the normal development of δ_{th}, Chen et al. [15] featured serpentine flow passages with Ω-shaped cross-sectional configurations for effective cooling of high concentration photovoltaic cells. They noticed an improvement in temperature uniformity in the cell module and a further decrease in cell temperature, presenting cell temperatures of 25-31°C, much lower than the fin heat sink's 45-63°C. Recently, Shiko and Al-Neama [28] have investigated numerically the thermal-hydrodynamic performance of a compound microchannel that consists of a circular cavity microchannel slotted from the top by a reentrant trapezoidal shape. Water was utilized as a working fluid, with volumetric flow rates (Q_{in}) ranging from 40 to 90 ml/min and the fluid inlet temperature adjusted to 20 °C. They observed that incorporating reentrant trapezoidal shapes can dramatically disturb both δ_{hy} and δ_{th}, as well as accelerate fluid flow and mixing in the main flow, resulting in considerable heat transfer augmentation.

To enhance convective heat transfer, there is a need for neoteric heat transport fluids with superior heat transfer properties, and nanofluids have been identified as viable alternatives to traditional heat transport fluids. Choi and Eastman [29] proposed a novel advanced potential coolant called nanofluid in 1995. The addition of nanoparticles typically modifies the base liquid's pre-existing thermal properties, such as density (ρ), specific heat (C_p), thermal conductivity (k), and viscosity (μ). These properties have the ability to significantly alter the heat transfer coefficient (h) within the mini/microchannels. Eastman et al. [30] stated that inserting 5% CuO nanoparticles improved k by approximately 60% when compared to pure water. This is due to Brownian motion, which is an important mechanism controlling the thermal behavior of nanoparticle-fluid suspensions. The second reason is the interfacial layer (nanolayer), which forms layered structures when liquid molecules near to a solid particle surface. These layered structures increase k by acting as a thermal bridge between nanoparticles and a bulk liquid [31]. In other words, as the nanolayer's thickness increases, so does its k.

Sajid et al. [32] performed an experimental study to investigate the hydrothermal characteristics of heat sinks with wavy microchannels using TiO_2/water nanofluids at various nanoparticle volume fraction (φ), Reynolds number (Re) in the laminar flow regime, and heating power. Their findings revealed that nanofluids had better-heated transfer characteristics than distilled water for all models tested. For example, using 0.012% TiO_2 nanofluids, the

lowest temperature of the surface and the most significant improvement in Nu_{avg} are 33.85°C and 40.57%, respectively. Khoshvaght-Aliabadi et al. [33] investigated a wavy MCHS with rectangular ribs and coolant made of Al_2O_3/H_2O nanofluids. Various rib arrangements (oblique and corner), waviness aspect ratios (0.025, 0.05, and 0.1), rib widths (0.1, 0.2, and 0.3mm), and *Re* ranging from 100 to 900 are investigated. The *h* and ΔP for the ribbed-wavy MCHSs were found to be 4% to 128% and 8% to 185% higher, respectively, than those for the smooth-wavy MCHSs. Their finding demonstrated that using nanofluids as a coolant increased the coefficient of thermal transfer and the ΔP when compared to pure water, and that their values increased as their volumetric concentration increased.

The hydrothermal performance of a MCHS with a wavy passage and nanofluids as a coolant was numerically examined by Naranjani et al. [34]. As a cooling agent, an Al_2O_3/water nanofluid with particle sizes of 29nm and 40nm and volume fractions (φ) of less than 4% was utilized, and its effect on the hydrothermal performance of a MCHS was compared to that of the base fluid for the *Re* ranged from 300 to 600. Their results revealed that using corrugated passages instead of conventional MCHS increases heat transfer by 24% to 36%, whereas the required pumping capacity rises by 20% to 31%, as a result of which overall performance improved by 16% to 24%. Saadoon et al. [35] recently compared 3D straight and wavy minichannel configurations with various nanoparticles dissolved in water, including CuO, Al_2O_3, Fe_3O4, TiO_2, and Ag. Three wave amplitudes (0.15, 0.2, and 0.25mm) are explored in their numerical simulations at various *Re* ranging from 200 to 1000 and a volume concentration (φ) variation ranging from 0 to 0.075. They observed that combining nanofluid and wavy minichannel could improve the heat sink's hydro-thermal performance. Ag/water nanofluid outperforms other nanofluids in heat transfer, with an increase of 54% in the *Nu* at a concentration volume of 0.075.

Recently, Ullah et al. [36] thoroughly reviewed and discussed the thermophysical characteristics of commonly used nanofluid correlations for ρ, C_p, k, and μ. They pointed out their constraints and the scope of their applicability. Kokate and Sonawane [37] experimentally investigated the impact of particle size (15nm and 60nm) and volume concentration (0.1 – 3%) on the thermal conductivity enhancement of Al_2O_3/water nanofluids. It was revealed that the nanofluid's thermal conductivity rises as the particle volume concentration increases and decreases as the particle size increases.

It can be indicated that utilizing curved or wavy microchannels, along with incorporating dimples and/or cavities on the sidewalls, can be an effective way to enhance forced convective heat transfer by reinitializing the δ_{th}, despite the possibility of increasing ΔP. In this research, two passive techniques are employed concurrently to augment the MCHS heat transfer efficacy: copper microchannels with a novel rectangular, trapezoidal, and semicircular-shaped reentrant cross-section configurations and fluid additives (nanofluids). The first technique significantly augments heat transfer by redeveloping both the δ_{hy} and δ_{th}, while the second technique improves the thermal properties of the base fluid. To the best of the authors' knowledge, none have ever been accomplished using a rectangular, trapezoidal, and semicircular-shaped reentrant cross-section MCHS with different kinds of nanofluids, which has essentially motivated the current work. The purpose of this study is to look into how different nanofluids with varying reentrant cross-section microchannel shapes affect the heat transfer performance of the MCHS. The main concerns are to examine the temperature distribution, Nu_{avg}, R_{th}, and ΔP of the MCHS with both water and nanofluids.

NUMERICAL METHODS

Physical Model

Three distinct and unique compound MCHSs are modelled in current study. Each proposed MCHS comprises of 15 parallel microchannels attached to the top surface of a copper block, with a footprint area ($W \times L$) of 20mm × 20mm and thickness (H) of 1.35mm. Every newly proposed microchannel has a bottom circular cavity with a diameter of 0.8mm that is slotted from the top in various shapes (namely rectangular, trapezoidal, or semicircular reentrant) to form reentrant microchannels. The copper substrate thickness (H_b) is fixed at a value of 0.25mm. The straight rectangular MCHS is chosen as the reference (denoted as Case_0), and the rectangular microchannel's detailed geometric parameters are as follows: the microchannel height (H_{ch}), width (W_{ch}) and length (L_{ch}) are 1.1mm, 0.6mm and 20mm, respectively. The microchannel's top surface is assumed to be covered by thermally insulating materials, while the bottom surface is subjected to a uniform heat flux (q) of 100W/cm^2. Figure 1 depicts the computational domain with geometrical parameters for three innovative MCHSs proposed beside the traditional one.

The first MCHS model proposed has a rectangular slot and is labeled Case_1, the second has a trapezoidal slot and is referred to as Case_2, and the last model has a semicircle slot and is denoted as Case_3. To minimize computing time, the current simulation uses only one symmetrical portion of the MCHS for all heat sink designs. In order to

Table 1. Specification of geometric parameters of four microchannels

Sample	A_{ch} (mm^2)	A_{ht} (mm^2)	P_{ch} (mm)	D_h (mm)
Case_0	0.6600	56	3.400	0.77647
Case_1	0.6296	56.0315	3.2016	0.78661
Case_2	0.6644	56.2402	3.3920	0.78350
Case_3	0.6486	58.1330	3.2989	0.78649

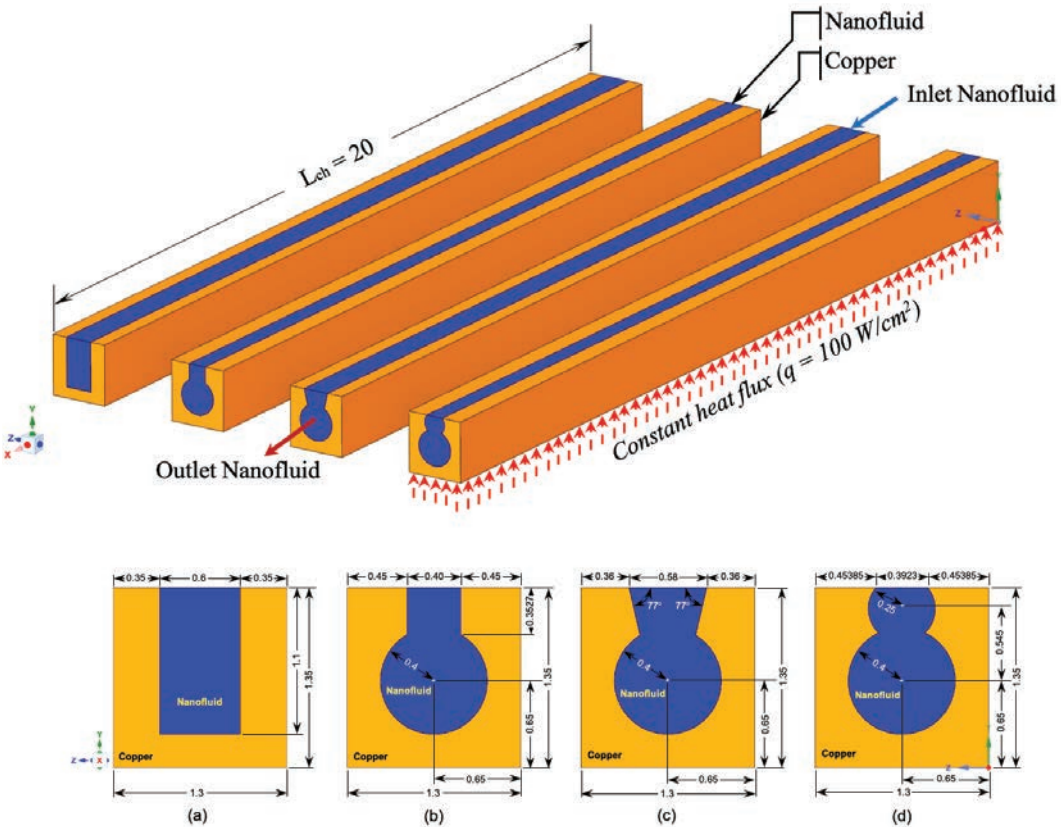

Figure 1. Schematic diagrams of compound microchannels proposed for (a) Case_0, (b) Case_1, (c) Case_2 and (d) Case_3 (All dimensions in mm).

make the comparisons possible, the microchannel hydraulic diameters (D_h) in various configurations had been identified as nearly identical and the same heat transfer surface areas (A_{ht}), as shown in Table 1.

Simulation Assumptions and Governing Equations

For numerical simulations, a finite volume method (FVM) in CFD FLUENT is employed. A three-dimensional (3D) conjugate heat transfer model with the following assumptions is used to analyze the effect of nanofluid on fluid flow and heat transfer through the MCHS with various reentrant arrangements:

(1) The fluid flow and heat transfer are both assumed to be in a steady state, and heat loss to the environment is completely ignored.
(2) The flow is laminar, and the fluid is single phase, Newtonian and incompressible.
(3) The effect of gravitational force, viscous dissipation and radiation heat transfer are negligible.
(4) Contact resistance is dismissed at the interfaces between the solid wall and the coolant.
(5) Smooth surface of the microchannel is selected.
(6) The thermal physical properties (i.e., density, specific heat, viscosity and thermal conductivity) of both the water and nanofluids are temperature-dependent, while temperature independent is considered for the MCHS material. User-defined functions (UDFs) were written in C^{++} language to account for temperature-dependence of the thermophysical properties of fluids and then imported to the FLUENT by interpreted UDFs.

Eqs. (1 – 4) show the governing equations for laminar, incompressible, and steady flow with conjugate heat transfer. Eqs. (1 – 3) represent the conservation of mass, momentum, and energy in the fluid domain, respectively. Eq. (4) denotes the steady-state heat conduction in the solid substrate.

$$\nabla \cdot \vec{V} = 0 \tag{1}$$

$$\rho_f \left(\vec{V} \cdot \nabla \vec{V}\right) = -\nabla p + \mu_f \nabla^2 \vec{V} \tag{2}$$

$$\rho_f C_{p,f} \left(\vec{V} \cdot \nabla T_f\right) = k_f \nabla^2 T_f \tag{3}$$

$$\nabla^2 T_s = 0 \tag{4}$$

where ρ_f, μ_f, k_f, $C_{p,f}$ and T_f represent the density, viscosity, thermal conductivity, the specific heat, and the absolute temperature of the coolant fluid, respectively. T_s is the solid temperature, and copper with a thermal conductivity (k_s), specific heat ($C_{p,s}$) and density (ρ_s) of 387.6W/(m.K), 381J/(kg.K) and 8978kg/m^3, respectively are selected in the current numerical simulation.

Computational Domain and Boundary Conditions

To simulate each of the four suggested MCHS configurations based on the assumptions stated previously, a unit cell with a single compound microchannel and a surrounding solid with the full flow length (20 mm) is selected as a computational domain, and the BCs must be assigned to obtain the simulation results. At the microchannel's inlet section, uniform fluid velocity (u_{in}) with different magnitudes and constant fluid temperature (T_{in} = 20°C) are configured. Since the Silicon chip's maximum working temperature is 125°C, the laminar flow regime can fulfill the heat dissipation requirements utilizing pure water as a coolant, so the *Re* range is chosen between 390 and 2075 ($20 \le Q_{in} \le 100$ *ml/min*). Pressure outlet BC with zero gradients at microchannel outlet is considered. The MCHS bottom surface is subjected to a constant heat flux BC of 100W/cm^2, while both of the numerical domain's lateral planes are set as symmetric BC. The microchannel's front and rear

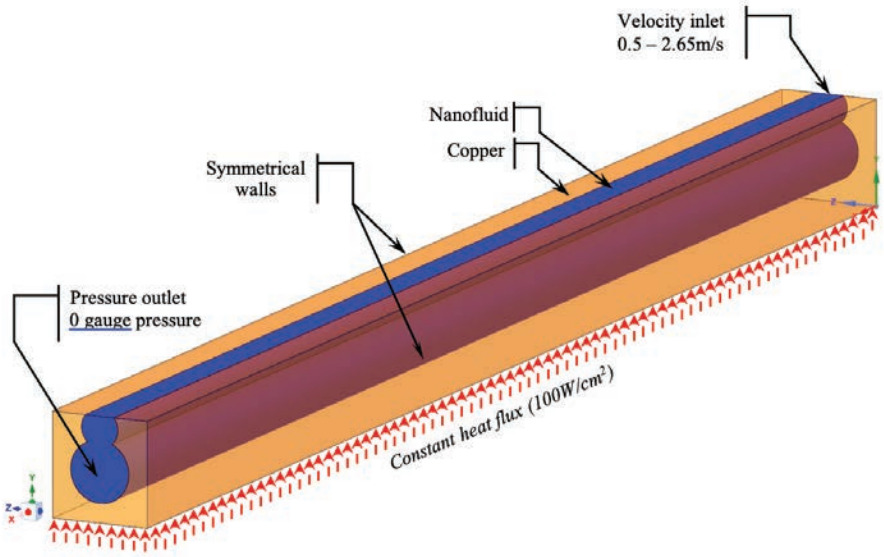

Figure 2. Circular MCHS with a semicircular-shaped reentrant cross-section configuration with boundary conditions.

Table 2. The boundary conditions used for simulation

Location	Hydrodynamic BCs	Thermal BCs
Channel inlet at $x = 0$	$u = u_{in}$ *and* $v = w = 0$	*For fluid:* $T_f = T_{in} = 20°C\ (293K)$ *For solid surface co − planar with the inlet:* $-k_s\left(\frac{\partial T_s}{\partial x}\right) = 0$
Channel outlet at $x = 20mm$	$P_f = P_{out} = 0\ (gauge\ pressure)$	*For fluid:* $-k_f\left(\frac{\partial T_f}{\partial x}\right) = 0$ *For solid surface co − planar with the outlet:* $-k_s\left(\frac{\partial T_s}{\partial x}\right) = 0$
The substrate's bottom wall at $y = 0$	$u = v = w = 0$	$-k_s\left(\frac{\partial T_s}{\partial y}\right) = q = 100\frac{W}{cm^2}$
Upper wall at $y = 1.35mm$	$u = v = w = 0$	$-k_s\left(\frac{\partial T_s}{\partial y}\right) = 0$
left and right walls: *At* $z = 0$ *and* $1.3mm$	⟝⟞	$-k_s\left(\frac{\partial T_s}{\partial z}\right) = 0\ (symmetry)$
Fluid/solid interface	$u = v = w = 0$	$T_s = T_f\ ;\ -k_s\left(\frac{\partial T_s}{\partial n}\right) = -k_f\left(\frac{\partial T_f}{\partial n}\right)$ where n is the coordinate normal to the wall.

sides, as well as the top surfaces of both liquid and solid, are assumed to be adiabatic surfaces to avoid contributing to overall heat transfer. The interfacial surfaces that exist between the fluid and solid domains are characterized as coupled interfaces, enabling energy to pass through them, and no-slip and no temperature–jump BCs are enforced. The BCs used for current study are presented in Figure 2, and can be summarized as shown in Table 2:

Data Acquisition

To analyze and compare the hydrothermal characteristics of various suspended nanoparticle types in compound microchannels, the following definitions are provided [9, 10]:

- The Reynolds number (*Re*) can be expressed as:

$$Re = \frac{\rho_f u_{in} D_h}{\mu_f} \tag{5}$$

where D_h denotes the microchannel hydraulic diameter based on the microchannel section, and can be determined as:

$$D_h = \frac{4A_{ch}}{P_{ch}} \tag{6}$$

where A_{ch} and P_{ch} denote the cross-sectional area and wetted perimeter of the microchannel, respectively.

- The steady-state sensible heat gain (Q) by the working fluid (Water) is given by:

$$Q = \rho_{bf} Q_{in} C_{p_{bf}} \left(T_{f,out} - T_{f,in}\right) = qA_h \tag{7}$$

where $T_{f,in}$ and $T_{f,out}$ represent the inlet and outlet bulk fluid temperatures, respectively. The ρ_{bf} and $C_{p_{bf}}$ are respectively the base fluid's density and specific heat capacity. The term Q_{in} (m^3/s) denotes the water volumetric flow rate. q and A_h indicate the effective constant heat flux per unit area (q = 100 W/cm^2) and the heated area (which, in the current study, represents the area of the microchannel bottom wall, ($A_h = 1.3 \times 20 mm^2$), respectively.

- The local convective heat transfer coefficient (h_x) can be calculated from the Newton's law of cooling as [38]:

$$h_x = \frac{qA_h}{A_{con}\left(T_{w_{(x)}} - T_{f_{(x)}}\right)} \tag{8}$$

A_{con} denotes the inner wall/fluid contact surface area available for convective heat transfer, and for the single straight rectangular microchannel can be computed as follows:

$$A_{con} = (W_{ch} + 2H_{ch})L_{ch} \tag{9}$$

$T_{w(x)}$ and $T_{f(x)}$ indicate the local conduction wall temperature and the local bulk fluid temperature, respectively, and can be determined as [38]:

$$T_{w_{(x)}} = \frac{1}{z}\int_z T_w(x,0,z)\,dz \tag{10}$$

$$T_{f_{(x)}} = \frac{\int_{A_{ch}} \rho_{bf} u(x,y,z) C_{p_{bf}} T_f(x,y,z) \cdot dA_{ch}}{\int_{A_{ch}} \rho_{bf} u(x,y,z) C_{p_{bf}} \cdot dA_{ch}} \tag{11}$$

- The local and average Nusselt number are determined by [38]:

$$Nu_x = \frac{h_x D_h}{k_{bf}} \tag{12a}$$

$$Nu_{avg} = \frac{1}{L}\int_L Nu_x \cdot dx \tag{12b}$$

- To evaluate heat dissipation performance, the total thermal resistance (R_{th}) of the MCHS can be used as [9, 10]:

$$R_{th} = \frac{T_{max} - T_{f,in}}{qA_h} \tag{13}$$

- The proposed design's overall performance is quantified using a thermal-hydraulic performance evaluation criteria (*PEC*) index or well-known performance factor (*PF*) that represents the average Nusselt number ratio (or the average heat transfer enhancement), E_{Nu}, over the total pressure drop ratio ($E_{\Delta P_t}$) to the power of one third as [9, 10]:

$$PF = \frac{Nu/Nu_o}{\sqrt[3]{\Delta P_t/\Delta P_{t,o}}} = \frac{E_{Nu}}{\sqrt[3]{E_{\Delta P_t}}} \tag{14}$$

The *PF* is defined as the ratio of the heat flow rate transferred to the system's required pumping power. The *PF* value denotes the level of thermal effectiveness in relation to total pressure drop (ΔP_t). The baseline Nusselt number (Nu_O) and total pressure drop ($\Delta P_{t,o}$) are obtained from the cases using conventional channels (which is Case_0 in the present work). If the value is greater than one, it indicates that thermal performance is superior to ΔP_t, and vice versa if the value is less than one. This parameter is used to compare the thermal and fluid-dynamic performances of compound microchannels with nanofluid to evaluate heat transfer enhancement.

Thermophysical Properties of the Base Fluid and Nanofluid

In the present analysis, liquid water is considered the working fluid baseline. The variation of all thermo-physical properties influencing the hydrodynamic characteristics with temperature is considered. For pure water, the temperature dependent density (ρ_{bf}) is offered by Thiesen–Scheel–Diesselhorst equation [39]. Temperature dependence of dynamic viscosity (μ_{bf}) is evaluated by Sherman

[40]. Moreover, specific heat capacity ($C_{p_{bf}}$) and thermal conductivity (k_{bf}) expressions with temperature are acquired from data polynomial fitting results [41].

$$\rho_{bf} = 1000\left[1 - \frac{T + 15.9414}{508929.2(T - 204.87037)}(T - 276.9863)^2\right] \quad (15)$$

$$\mu_{bf} = 2.414 \times 10^{-5} \times 10^{\left(\frac{247.8}{T-140}\right)} \quad (16)$$

$$\begin{aligned} C_{p_{bf}} = {} & 198532 - 2894.85T + 17.2363T^2 \\ & - 5.12699 \times 10^{-2}T^3 + 7.61613 \times 10^{-5}T^4 \\ & - 4.51782 \times 10^{-8}T^5 \end{aligned} \quad (17)$$

$$\begin{aligned} k_{bf} = {} & -1.579 + 0.01544T - 3.515 \times 10^{-5}T^2 \\ & + 2.678 \times 10^{-8}T^3 \end{aligned} \quad (18)$$

where ρ_{bf}, μ_{bf}, $C_{p_{bf}}$ and k_{bf} are density, dynamic viscosity, specific heat and thermal conductivity of the base fluid (water), respectively. The unit of T is K in Eqs. (15–18).

One important variable in nanofluid studies is nanofluid volume fraction (φ), which is defined as the constituent volume divided by all constituent volumes of the mixture prior to mixing [42], and can be calculated as:

$$\varphi = \frac{V_{np}}{V} = \frac{V_{np}}{V_{np} + V_{bf}} \quad (19)$$

where V stands for total volume of solution, while V_{bf} and V_{np} are base fluid and nanoparticle volumes, respectively. Volume concentration (φ) has a significant effect on the thermophysical parameters of nanofluids (Dynamic viscosity, thermal conductivity, specific heat, and density), hence it is vital in nanofluid applications. The thermophysical properties of the nanofluid can be expressed as follows:

The effective density of nanofluid (ρ_{nf}) that proposed by Pack and Cho [43] is determined as:

$$\rho_{nf} = (1 - \varphi)\rho_{bf} + \varphi\rho_{np} \quad (20)$$

The specific heat of nanofluid ($C_{p_{nf}}$) that proposed by Khanafar [44] and Buongiorno [45] assumed thermal equilibrium between the particles and the fluid, and can be written as:

$$C_{p_{nf}} = \frac{(1 - \varphi)\left(\rho C_p\right)_{bf} + \varphi\left(\rho C_p\right)_{np}}{\rho_{nf}} \quad (21)$$

ρ_{np} and $C_{p_{np}}$ refer to density and specific heat of nanoparticle, respectively. The effective thermal conductivity (k_{eff}) that determined by Corcione [46] after took data from over 13 different sources of CuO, Al_2O_3 and TiO_2 particles with base liquids of water and ethylene glycol (EG) is given as:

$$k_{eff} = k_{bf}\left[1 + 4.4Re_{np}^{0.4}Pr_{bf}^{0.66}\left(\frac{T_{nf}}{T_{fr}}\right)^{10}\left(\frac{k_{np}}{k_{bf}}\right)^{0.03}\varphi^{0.66}\right] \quad (22)$$

where Re_{np} is the nanoparticle Reynolds number while Pr_{bf} is the Prandtl number of the base fluid. T_{nf} and T_{fr} are respectively the nanofluid temperature and the freezing point of the base fluid in Kelvin (about 273.15K), k_{np} is the nanoparticle thermal conductivity. The effect of dimensionless numbers such as Re_{np} and Pr_{bf} as the temperature changed in the model was considered by Corcione, and can be expressed as:

$$Pr_{bf} = \frac{\mu_{bf}C_{p_{bf}}}{k_{bf}} \quad (23)$$

$$Re_{np} = \frac{\rho_{bf}u_B d_{np}}{\mu_{bf}} \quad (24)$$

where d_{np} and u_B are the nanoparticle diameter and the nanoparticle mean Brownian velocity, respectively. Assuming no agglomeration, u_B can be estimated as the ratio of d_{np} to the time (τ_D) required to cover such distance, which, according to Keblinski et al. [47], is:

$$\tau_D = \frac{d_{np}^2}{6D} = \frac{\pi\mu_{bf}d_{np}^3}{2K_BT} \quad (25)$$

where D is the Einstein diffusion coefficient and K_B denotes the Boltzmann's constant (K_B = 1.38066 x 10^{-23} J/K). Henc u_B can be determined as:

$$u_B = \frac{2K_BT}{\pi\mu_{bf}d_{np}^2} \quad (26)$$

Substituting Eq. (26) into Eq. (24) we can get:

$$Re_{np} = \frac{2\rho_{bf}K_BT}{\pi\mu_{bf}^2 d_{np}} \quad (27)$$

The nanofluid effective dynamic viscosity (μ_{eff}) proposed by Corcione [46] was obtained using a wide selection of experimental data available in the literature. These data are for nanofluids containing alumina, titania, silica, and copper nanoparticles suspended in water, EG, and ethanol (Eth), with diameters ranging from 25nm to 200nm, volume fractions ranging from 0.01% to 7.1%, and temperatures ranging from 293K to 333K.

$$\mu_{eff} = \mu_{bf}\left(\frac{1}{1 - 34.87\left(\frac{d_{np}}{d_f}\right)^{-0.3}\varphi^{1.03}}\right) \quad (28)$$

where d_f is the equivalent diameter of a base fluid molecule, and given by:

$$d_f = \sqrt[3]{\frac{6M}{N\pi\rho_{bf_o}}} = \sqrt[3]{\frac{6 \times 18.01528 \times 10^{-3}}{6.022 \times 10^{23} \times \pi \times 998.26}} = 3.8538 \times 10^{-10}\ m \quad (29)$$

in which M is the molecular weight of the base fluid and equal to 18.01528 [g/mole], N is the Avogadro number and equal to 6.022×10^{23} [1/mole], and ρ_{bf_o} is the mass density of the base fluid calculated at temperature T_o = 293K. In this study, Al_2O_3 and CuO nanoparticles were chosen to dispersion in water to form a nanofluid. The reason for adopting these two nanoparticles is that they have unique properties that make them superb for improving heat transfer performance, specifically high thermal conductivity. The thermophysical properties of Al_2O_3 and CuO nanoparticles at temperature of 20°C are listed in Table 3 [48].

Grid Sensitivity

After geometry of four models created by a SpaceClaim tool, a structured mesh for the solver was generated using the ANSYS software 2022R1. In the simulation, the structured mesh was considered in all zones, with hexahedral mesh being used. The governing equation is discretized using the FVM. A mesh independence analysis was performed for all MCHS models before beginning to create the CFD production runs. The procedure starts with a coarse mesh and refines it on a regular basis until the differences in the findings are less than a pre-determined acceptable error. A grid independence test was performed to determine the optimum structured mesh for producing accurate results with lower time cost. The grid number for each MCHS design considered are listed in Table 3.

The relative error between the finest grids (F_1) and other grids (F_2) is determined according to the following equation:

$$e\% = \left|\frac{F_2 - F_1}{F_1}\right| \times 100 \tag{30}$$

where F might be any parameter like temperature, average Nusselt number (Nu_{avg}), or pressure drop (ΔP). From Table 4, it can be seen that the Nu_{avg} is tending to be stable after mesh element size is 0.03mm, where further refinement did not change the result by more than 0.8% which was taken as an appropriate mesh quality for computation, considering better accuracy and less computational effort.

Table 3. Nanoparticle properties at temperature of 20°C [48]

Nanoparticle	$\rho\left(\frac{kg}{m^3}\right)$	$C_p\left(\frac{J}{kg.K}\right)$	$k\left(\frac{W}{m.K}\right)$	$\mu\left(\frac{kg}{m.s}\right)$
Al_2O_3	3600	765	36	—
CuO	6510	540	18	—

Table 4. Mesh independence test at Q_{in} = 60 *ml/min* (*or* 1 cm^3/sec)

Five meshing methods and simulation results for Case_0					
Method	I	II	III	**IV**	V
Minimum element size [mm]	0.045	0.04	0.035	**0.03**	0.025
Number of grids	386,280	561,000	823,953	**1,320,660**	2,246,400
Nu_{avg}	23.3868	23.8532	24.1821	**24.4285**	24.5951
%Error	4.913	3.016	1.680	**0.677**	—
Five meshing methods and simulation results for Case_1					
Method	I	II	III	**IV**	V
Minimum element size [mm]	0.045	0.04	0.035	**0.03**	0.025
Number of grids	478,188	711,500	1,016,380	**1,644,155**	2,796,000
Nu_{avg}	24.4348	24.8381	25.1829	**25.5387**	25.7241
%Error	5.012	3.444	2.104	**0.721**	—
Five meshing methods and simulation results for Case_2					
Method	I	II	III	**IV**	V
Minimum element size [mm]	0.045	0.04	0.035	**0.03**	0.025
Number of grids	504,828	727,500	1,052,353	**1,666,166**	2,911,200
Nu_{avg}	23.8705	24.1915	24.6067	**24.9874**	25.1834
%Error	5.213	3.939	2.290	**0.778**	—
Five meshing methods and simulation results for Case_3					
Method	I	II	III	**IV**	V
Minimum element size [mm]	0.045	0.04	0.035	**0.03**	0.025
Number of grids	503,940	714,500	1,098,033	**1,701,517**	2,958,400
Nu_{avg}	24.1106	24.4783	24.8249	**25.1997**	25.3908
%Error	5.042	3.594	2.229	**0.753**	—

RESULTS AND DISCUSION

Validation and Verification

The numerical computation is accomplished by solving the governing conservation equations based on the BCs. The finite-volume approach is used to discretize the governing equations for all domains. To achieve the pressure-velocity coupling, the coupled algorithm method was used. Simultaneously, the second order upwind scheme is being used for both the convective and the diffusion terms. Furthermore, convergence criterions are set to be less than 10^{-6} for both continuity and velocity, while less than 10^{-9} for energy.

The current work was validated in relation to the MCHS used in the numerical work of **Qu and Mudawar** [50], which matched the one used in Kawano et al.'s experimental work [49]. Further experimental and numerical details can be found in the Ref. [50]. The validation was performed on a silicon MCHS having microchannels with a width of 57μm and a depth of 180μm, that are separated by a 43μm wall. Water was used as the cooling fluid, with the inlet Reynolds number set to be constant at 140 and the temperature set to 20°C. A constant heat flux (q) of 90W/cm^2 was subjected at the MCHS's top wall. To take advantage of symmetry, a unit cell with only one straight rectangular microchannel and the surrounding solid was selected for numerical simulation using the same boundary conditions as Qu and Mudawar's work [50]. The fluid bulk temperature and average wall temperatures at the MCHS top and bottom walls are plotted as functions of longitudinal distance x as shown in Figure 3. As can be seen, all temperature predictions agree well with Qu and Mudawar's work, with a maximum discrepancy of less than 0.8%. As a result, the numerical method adopted is extremely reasonable and accurate. Therefore, the current numerical code can accurately predict the basic characteristics of fluid flow and heat transfer within the MCHS.

Effect of MCHS Geometry and Nanofluids On Pressure Drop and Fluid Flow

To fully comprehend the MCHS's liquid flow and heat transport, numerical simulations are accomplished for various MCHS configurations using two different nanoparticles (Al_2O_3 and CuO) suspended in water as a base fluid with a volume concentration (φ) of 4%. In the MCHS analysis, pressure drop (ΔP) is an important parameter. It determines how much pumping power is required to deliver coolant through heat sink channels. Figure 4 shows the impact of both nanofluids (Al_2O_3/water and CuO/water) and water flow rates ($20 \le Q_{in} \le 100$ *ml/min*) on the total pressure drop (ΔP_t) for four different configurations of MCHS models. As expected, ΔP_t increases rapidly with Q_{in}, as can be noted in all cases. This is simply because the momentum boundary layer thickness increases as the fluid velocity increases, resulting in a larger friction loss during fluid flow within microchannels. This behavior is unaffected by whether the fluid used is pure water or nanofluids.

For pure water ($\varphi = 0$), it is evident from Figure 4 that the Case_1 has a higher ΔP_t than the other MCHSs, while the second and third highest ΔP_t were seen in the Case_3 and

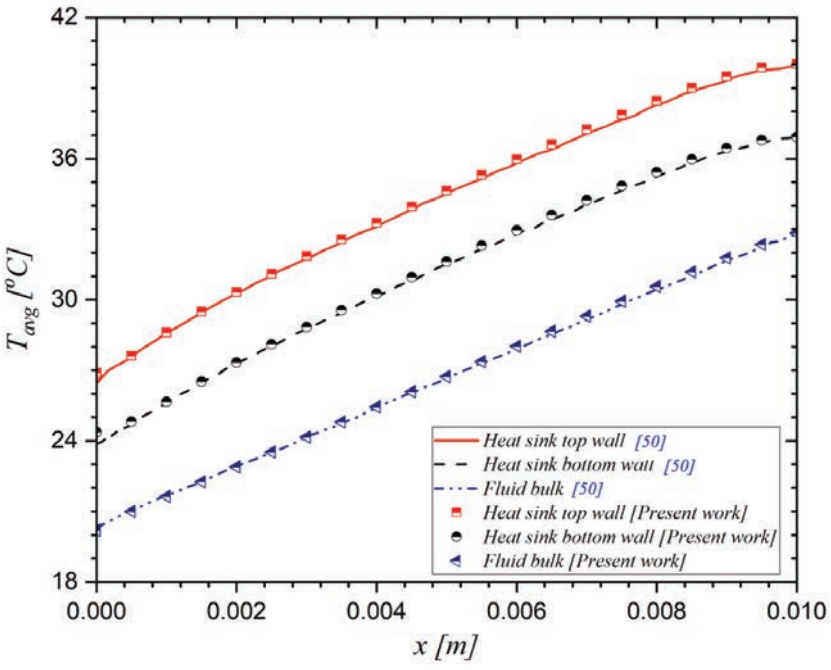

Figure 3. Comparison between numerical simulations and numerical predictions the Qu and Mudawar's work [50] on the average temperature in a straight rectangular microchannel along x direction.

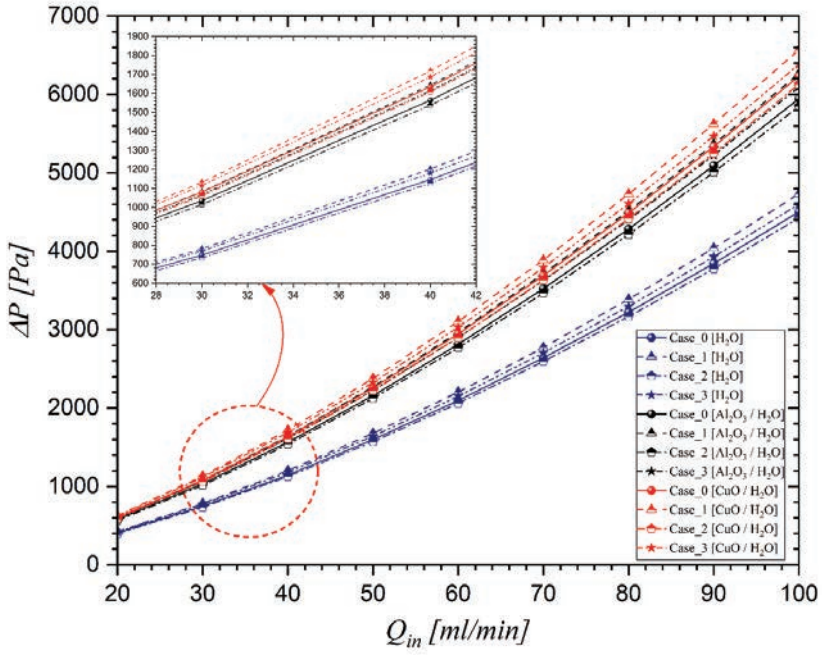

Figure 4. Effect of Q_{in} and nanofluids on the ΔP_t for four different MCHS configurations.

Case_0 (the traditional MCHS), respectively, while Case_2 has the lowest ΔP_t. At the highest volumetric flowrate (Q_{in} = 100 *ml/min*), ΔP_t in Case_1 and Case_3 increased by 5.11% and 2.14%, respectively, compared to Case_0, while Case_2 decreased by 1.74%. For nanofluids (φ = 4%), an increasing trend in ΔP_t was observed, with CuO/water nanofluid producing the highest pressure. For example, at Q_{in} = 100 *ml/min*, Case_1 with CuO/water nanofluid had the highest ΔP_t of 6567.73Pa, followed by Case_3 with 6384Pa, and Case_1 with Al_2O_3/water nanofluid had the third highest ΔP_t of 6265.3Pa, while Case_0 and Case_2 with CuO/water nanofluid have the fourth and fifth highest ΔP_t of 6233.46Pa and 6128.8Pa, respectively, whereas Case_3, Case_0, and Case_2 with Al_2O_3/water nanofluid had ΔP_t values of 6095.1Pa, 5945.76Pa, and 5847Pa, respectively. When compared to water, nanofluids demonstrated a greater pressure drop. With the addition of nanoparticles to the base fluid, the friction factor increases due to an increase in the working fluid's viscosity.

The pressure drop contours for the four MCHS models using pure water and nanofluids (Al_2O_3/water and CuO/water with φ = 4%) as coolant are shown in Figure 5. For each MCHS case, five cross-sectional planes were presented at *xx* = 0, 1, 2, 3, and 4mm from the entrance region. These contours are taken with Q_{in} = 60 *ml/min*, fluid inlet temperature of 20°C, and an input power (*Q*) of 26W (q = 100 W/cm^2) applied on the MCHS bottom side.

Overall, Pressure declines along the flow direction, but pressure rises locally along the flow direction in the reentrant part. It is clearly seen that Case_1 and Case_3 create a slightly larger ΔP_t than the other two cases (Case_0 and Case_2). This is due to the fact that the narrow slot restriction yielded a higher friction resistance for liquid flow in compound MCHSs, while the main fluid particles had a tendency to travel through the circular cavity. Hence, the compound microchannels expanded the hydrodynamically developing flow and intensified fluid mixing in the inlet zone, resulting in a higher frictional pressure loss and, as a result, inducing a ΔP when compared to traditional MCHS (Case_0). It is obvious that adding nanoparticles to water increases suspension viscosity and density, resulting in an increase in ΔP. Because of the van der Waals forces between the nanoparticles and the base fluid, when they are mixed, the nanoparticles tend to scatter and form nanoclusters. The movement of base fluids on each other will be prevented due to the formation of agglomerations; hence, the viscosity of nanofluid will increase.

To assess the effect of each suggested geometry design on the MCHS hydrothermal performance with and without two different kinds of nanofluids, a comparison was performed by referring to the streamlines and velocity contour distribution on the (*y* - *z*) plane at the outlet microchannel region (x = 20 *mm*) for Q_{in} = 60 *ml/min*.

Figure 6 demonstrates the velocity streamlines together with the velocity contour of all cases at the outlet's cross-section plane, in which the Q_{in} was set to 60 *ml/min* at $T_{f,in}$ = 20°C, and q = 100W/cm^2. It is obvious that Case_1 has superior flow velocity that other cases, while the traditional one (Case_0) has the lowest flow velocity. Because the compound microchannels have a large bottom circular cavity and a restricted exit slot attached to the circular cavity's crest, the cramped slot restricts fluid flow, like a nozzle. The

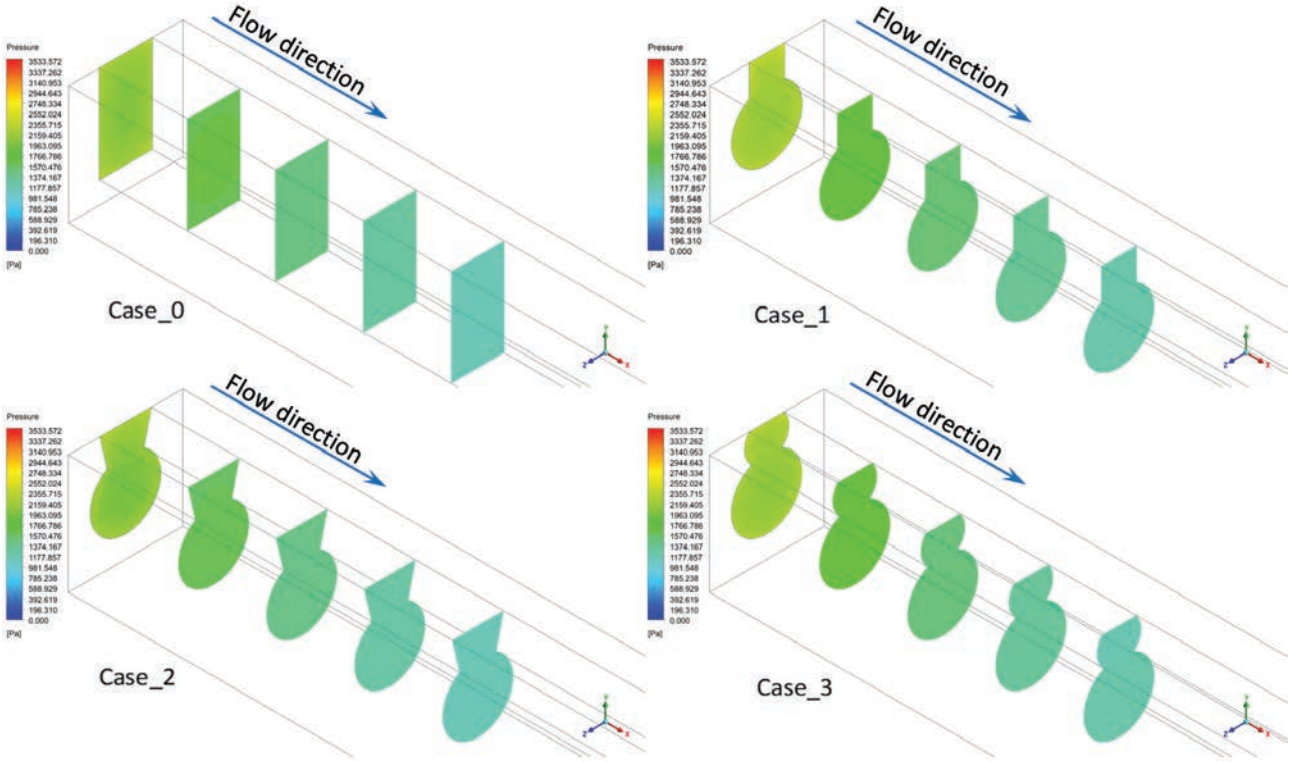
Flow direction
Case_0
Flow direction
Case_1
Flow direction
Case_2
Flow direction
Case_3

(a)

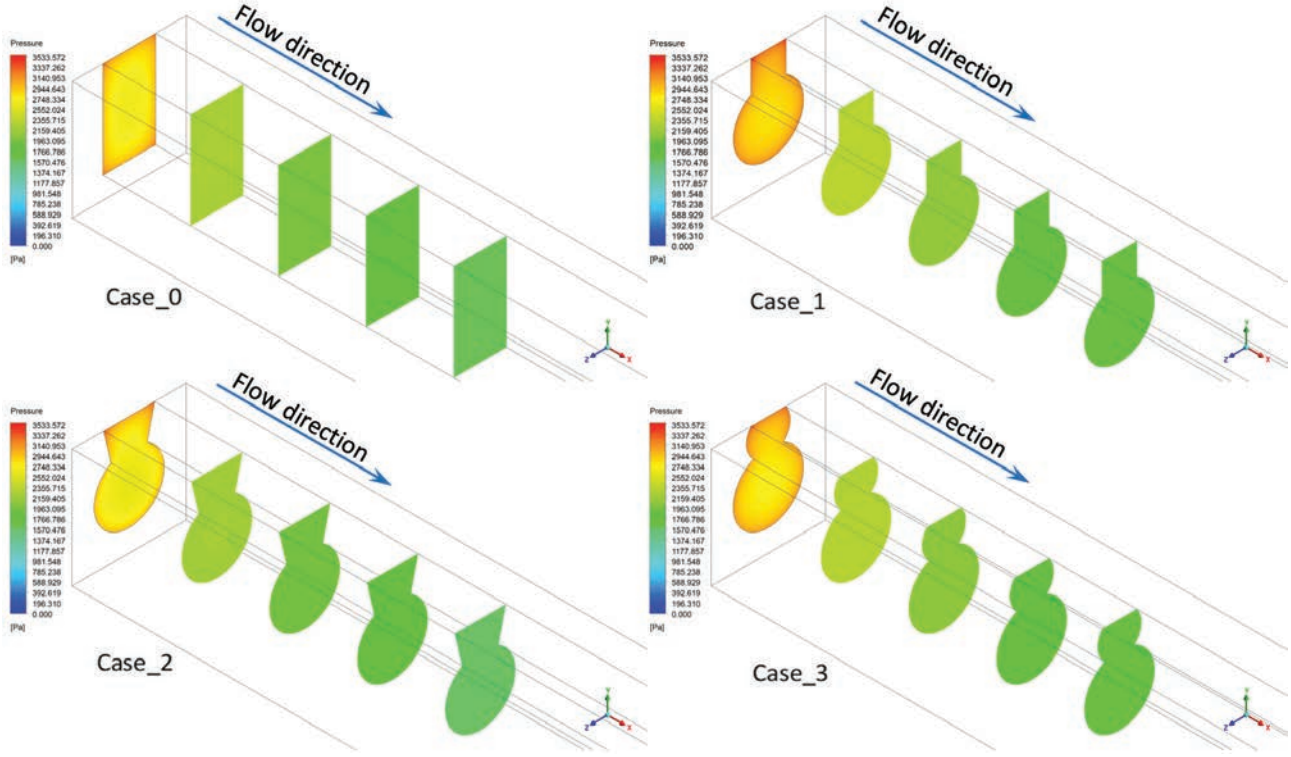
Flow direction
Case_0
Flow direction
Case_1
Flow direction
Case_2
Flow direction
Case_3

(b)

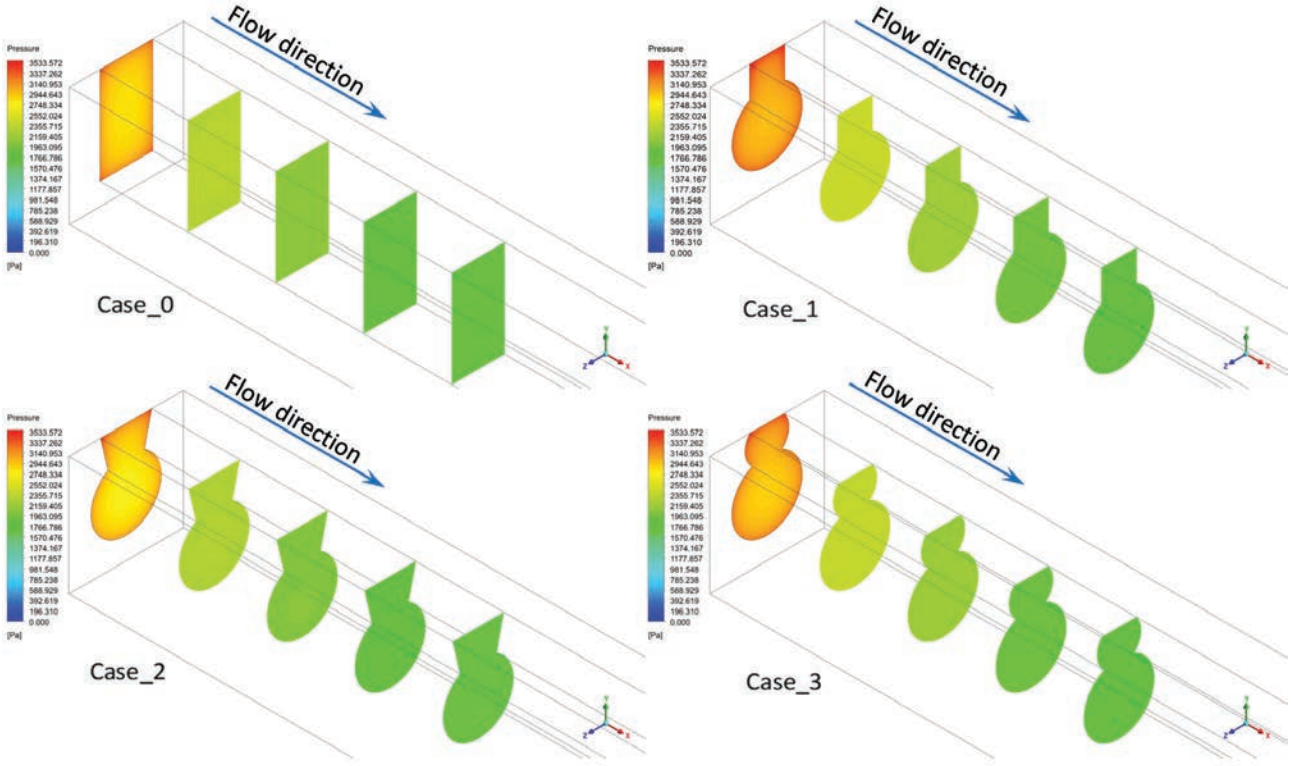

(c)

Figure 5. Comparison of pressure drop contours for different geometric structures on the *y* - *z* plane (*x* = 0, 1, 2, 3 *and* 4 *mm*) at the entrance region at Q_{in} = 60 *ml/min* for (a) H_2O, (b) Al_2O_3/H_2O and (c) CuO/H_2O.

cross section's continuous velocity streamlines were disrupted by the abrupt protrusion formed by the junction of the circular cavity and the vertical slot. The fluid particles were throttled as a result, and the by-pass flow in the confined slot was separated from the main flow in the circular cavity. Despite the fact that the by-pass flow velocity in the narrow slot was reduced, throttling effects intensified the main flow in the circular cavity. The fluid particle acceleration increased momentum transport and intensified convection heat transfer in the main flow.

Effect of MCHS Geometry and Nanofluids on Temperature Distribution and Heat Transfer

Figure 7 demonstrates how nanofluids (Al_2O_3/water and CuO/water) and water flow rates ($20 \le Q_{in} \le 100$ *ml/min*) affect maximum wall temperatures (T_{max}) for four different MCHS model configurations. As can be seen, when Q_{in} is increased, T_{max} decreases monotonically, and using nanofluids as a coolant has superior effect on decreasing the microchannel base temperature to which the integrated circuit (IC) is adhered.

For pure water (φ = 0), it is obvious from Figure 7 that Case_3 has the lowest T_{max} than the other MCHS, followed by Case_1 and Case_2, while Case_0 (the traditional MCHS) exhibits higher T_{max}. At the highest volumetric flowrate (Q_{in} = 100 *ml/min*), T_{max} in Case_3 (68.27°C) decreased by 3.2% compared to Case_0 (70.53°C), while Case_1 (68.8°C) and Case_2 (69.93 °C) decreased by 2.45% and 0.85%, respectively.

For nanofluids (φ = 4%), a decreasing trend in T_{max} was observed, with CuO/water nanofluid producing the lowest T_{max}. For example, at Q_{in} = 100 *ml/min*, Case_3 with CuO/water nanofluid had the lowest T_{max} of 61.56°C, followed by Case_1 and Case_2 with T_{max} of 61.97°C and 62.86°C, respectively, when CuO/water nanofluid was also used. Case_3 and Case_1 with Al_2O_3/water nanofluid had the fourth and fifth lowest T_{max} values of 62.9°C and 63.32°C, respectively, while Case_0 with CuO/water nanofluid had the seventh lowest T_{max} of 63.34°C, whereas the last values of T_{max} being 64.23°C with Case_2 and 64.75°C with Case_0 when Al_2O_3/water nanofluid was used.

The comparison of the 3-D temperature distributions of compound (Case_1, 2, and 3) and traditional (Case_0) MCHSs reveals that compound microchannels have lower wall temperatures, as shown in Figure 8. For four different microchannel configurations, the five cross-sectional planes at the longitudinal flow's second half region on the *y* - *z* plane (*x* = 12, 14, 16, 18 and 20mm) from the entrance region at Q_{in} = 60 *ml/min*, an inlet temperature of 20°C, and a heat flux (q) of 100W/cm² were presented here. In all microchannels, it can be claimed that the temperature

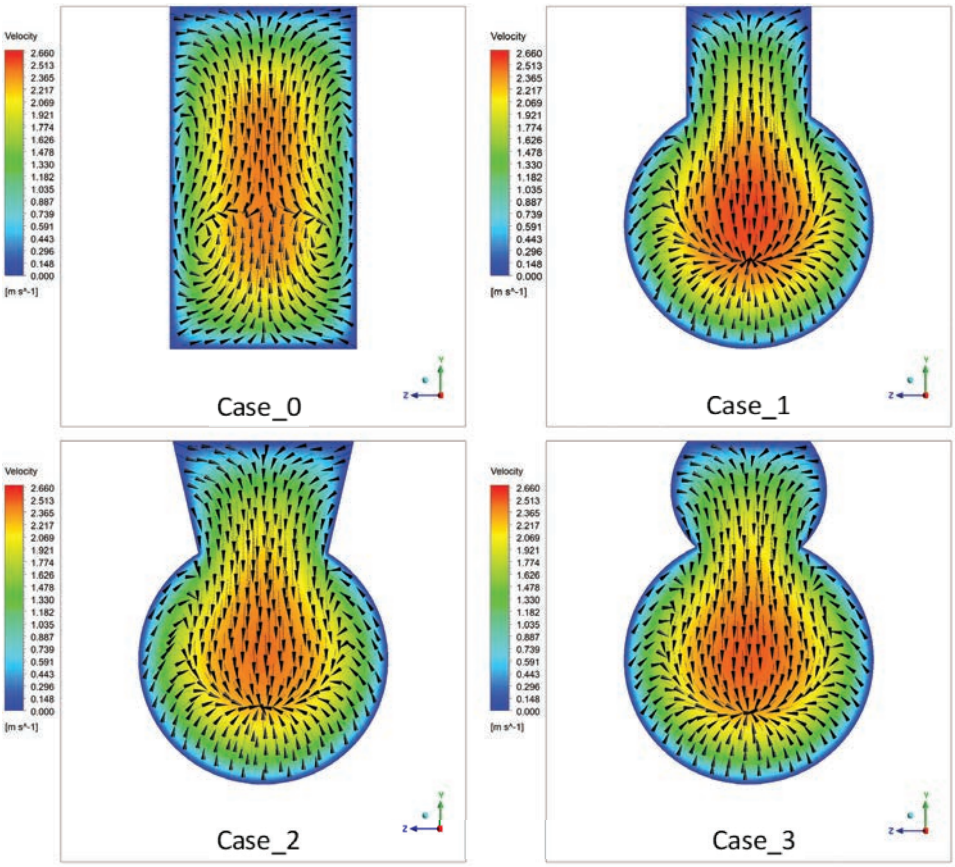
Velocity
2.660
2.513
2.365
2.217
2.069
1.921
1.774
1.626
1.478
1.330
1.182
1.035
0.887
0.739
0.591
0.443
0.296
0.148
0.000
[m s^-1]
Case_0
Case_1
Case_2
Case_3

(a)

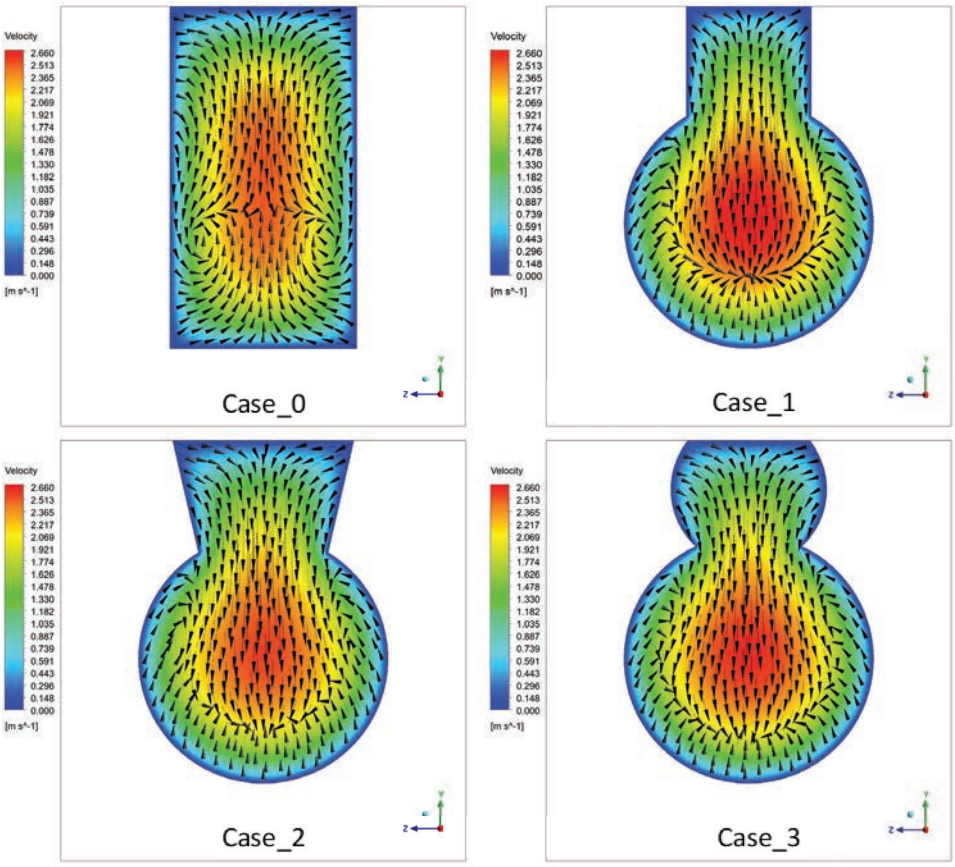
Velocity
2.660
2.513
2.365
2.217
2.069
1.921
1.774
1.626
1.478
1.330
1.182
1.035
0.887
0.739
0.591
0.443
0.296
0.148
0.000
[m s^-1]
Case_0
Case_1
Case_2
Case_3

(b)

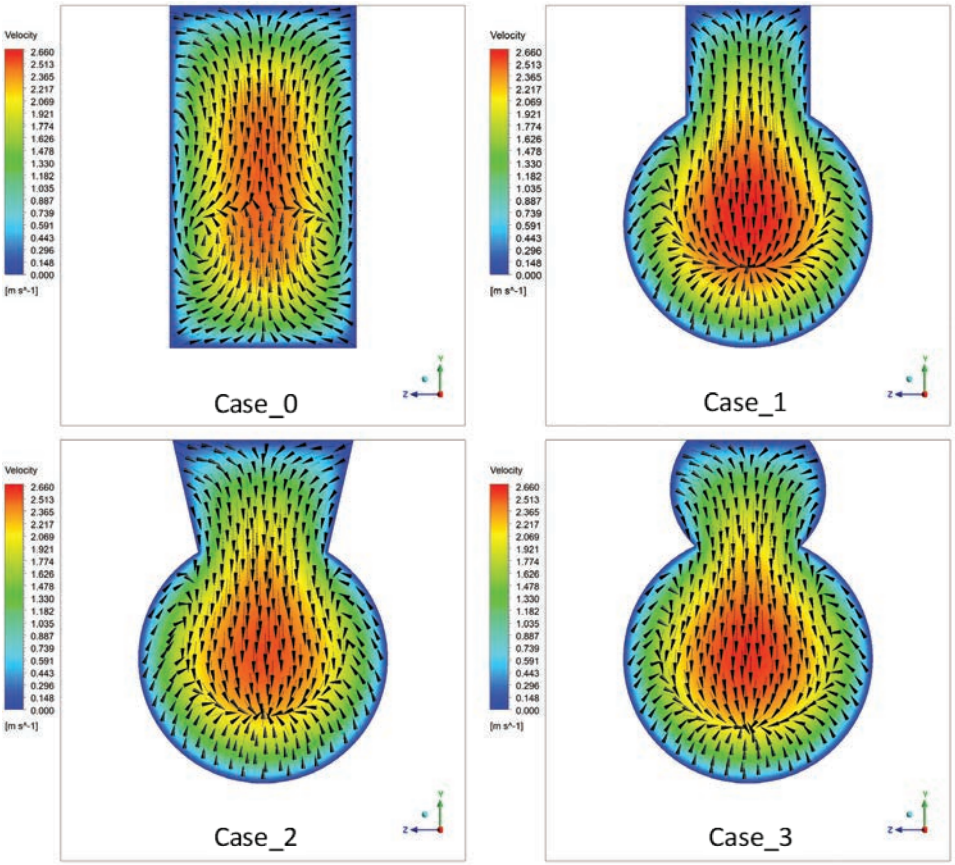

(c)

Figure 6. Streamlines and velocity contour distribution for different geometry structure on y - z plane (x = 20 *mm*) at the outlet microchannel region with Q_{in} = 60 *ml/min* for (a) H_2O, (b) Al_2O_3/H_2O, and (c) CuO/H_2O.

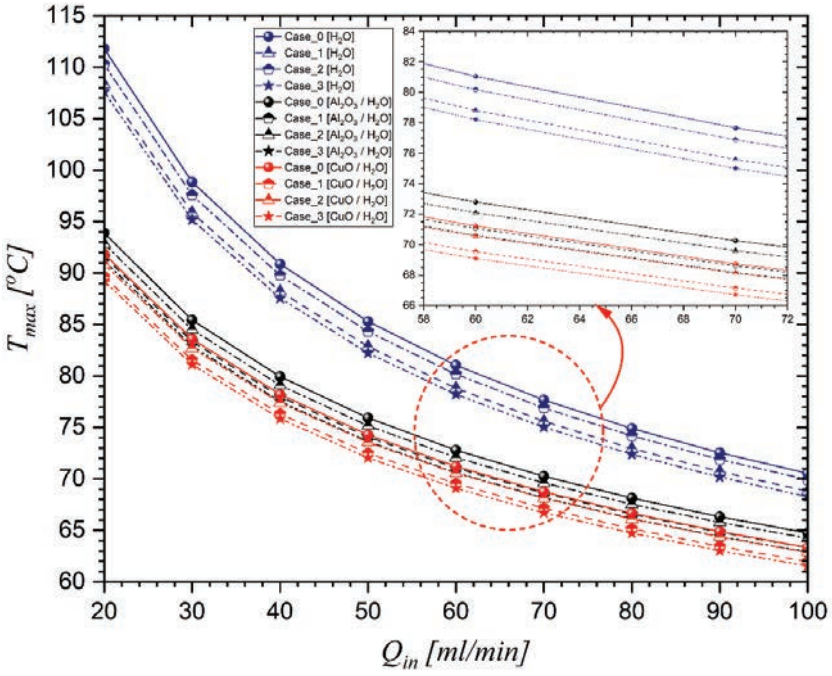

Figure 7. Effect of Q_{in} and nanofluids on the maximum wall temperatures for four different MCHS configurations.

gradient between liquid close to the wall and core liquid increased as the flow moved downstream. Notwithstanding, the distribution of side wall temperature along the flow stream of compound MCHSs was lower than that of the straight rectangular MCHS, indicating that the temperature of the compound microchannels' side walls in the simulations was about 2–9°C lower than the Case_0 model at the same x location. Furthermore, the liquid temperature profile inside compound MCHSs was affected by the microchannels' reentrant configurations.

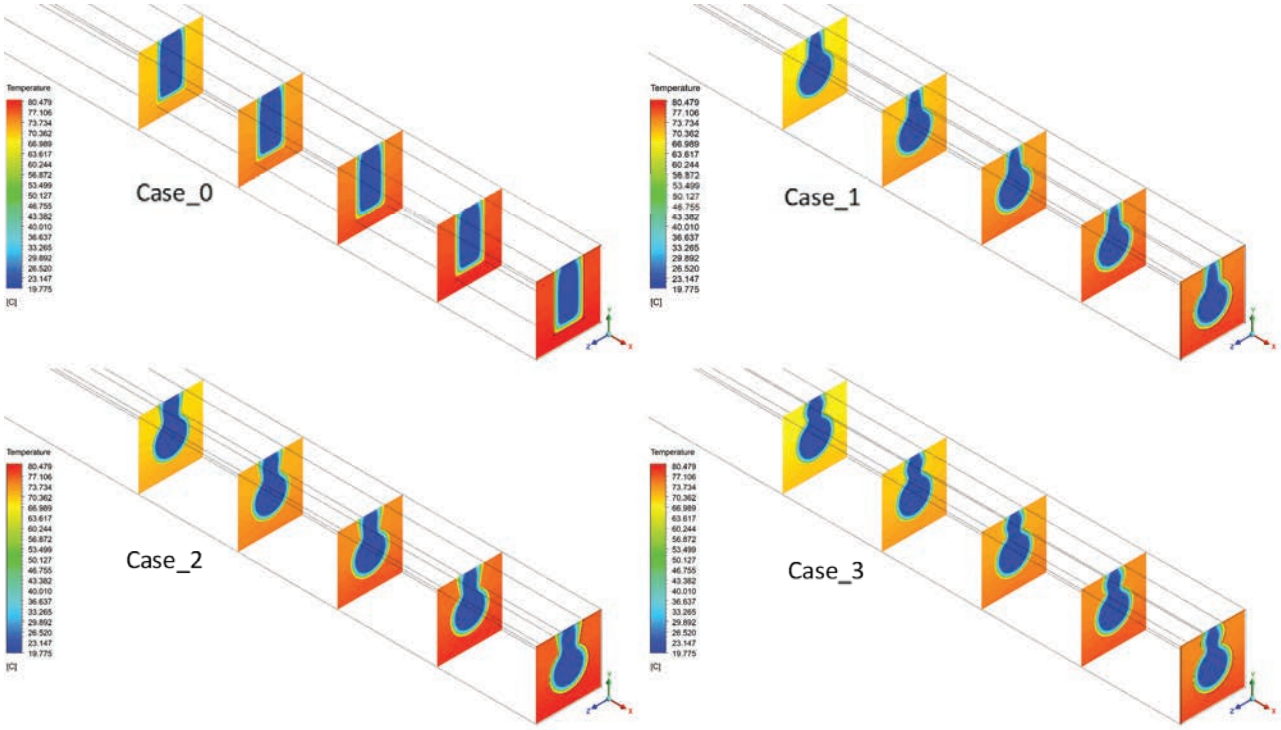

(a)

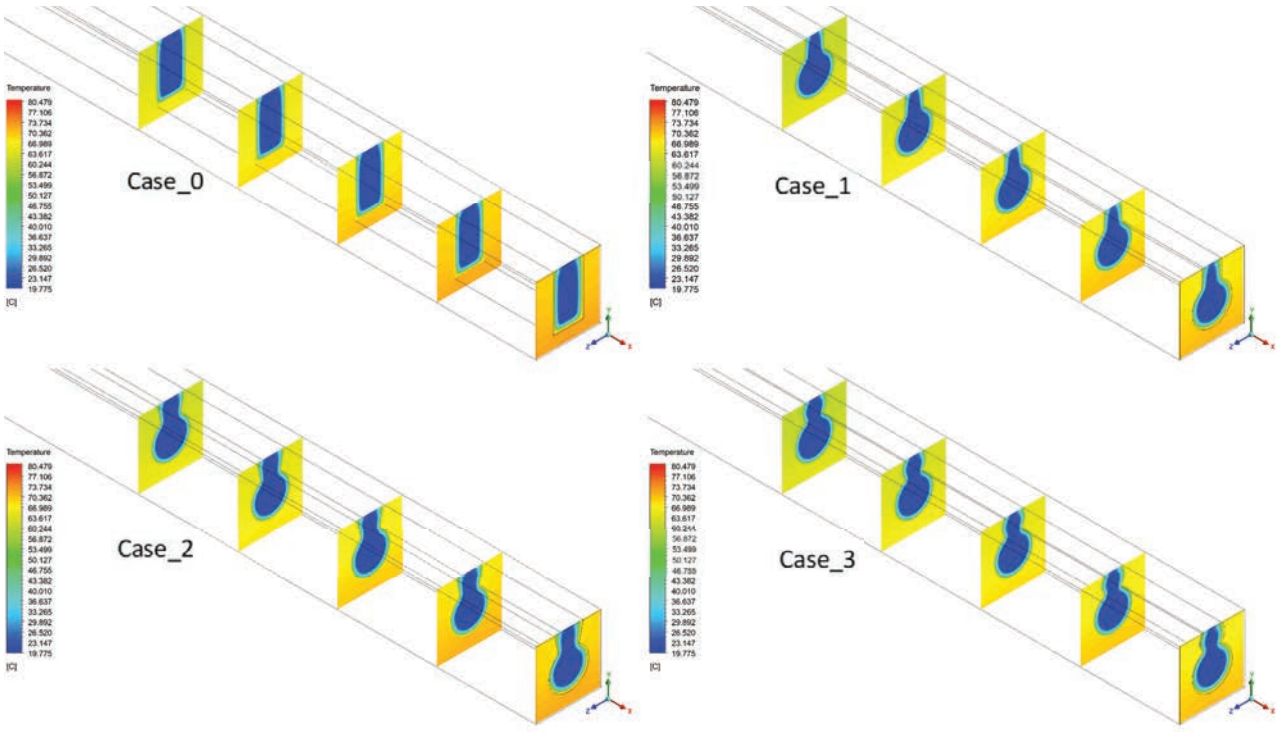

(b)

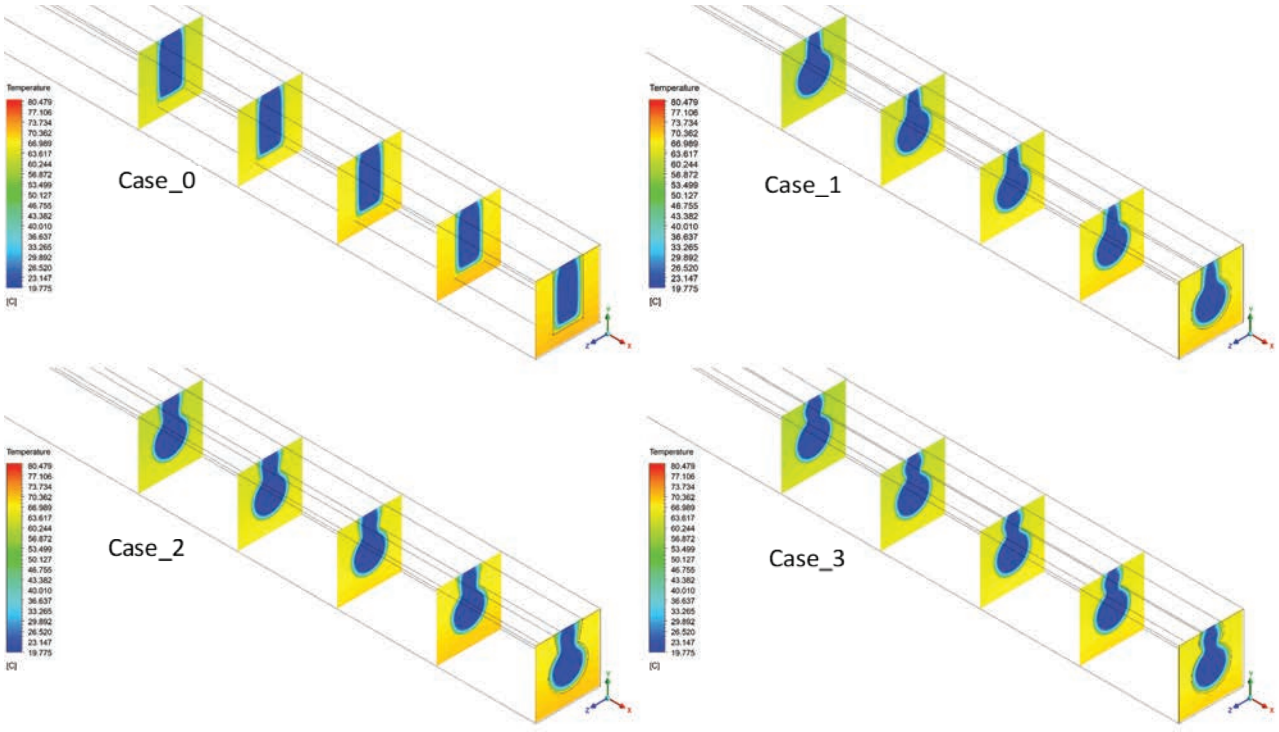

(c)

Figure 8. Comparison of 3D temperature distribution for different geometric structures on the *y* - *z* plane (*x* = 12, 14, 16, 18 *and* 20 *mm*) from the entrance region at Q_{in} = 60 *ml/min* for (a) H_2O, (b) Al_2O_3/H_2O, and (c) CuO/H_2O.

The inclusion of nanoparticles into the base fluid, on the other hand, results in enhanced heat transfer exchange between the fluid and microchannel wall. While heat transfer enhancement for the base fluid is not particularly significant. Additionally, the inclusion of reentrant increased the *h* by increasing turbulent intensity and flow mixing. It is worth noting that using CuO/water nanofluid can significantly reduce the MCHS wall temperature, this is due to the nanofluid's *k* and ρ are increasing.

Figure 9 portrays temperature contours at the outlet's cross-section plane for all MCHS models at Q_{in} = 60 *ml/min*. In contrast to the straight rectangular microchannel (Case 0), the protrusion of compound microchannels disrupted the continuous temperature contours of fluid in Cases 1, 2, and 3. The abrupt protrusion at the circular cavity's intersection and the upside slot disrupted the normal development of the δ_{th} from bottom to top in the flow passages' cross section, which resulted in two segments of both hydrodynamic and thermal boundary regions. The flow separation caused by the throttling effect, as stated previously, resulted in a thinner δ_{th} of the main flow in the circular cavity, particularly at the transition zone from the circular cavity to the slot. The disruption of the δ_{th}, as well as the fluid flow acceleration and mixing in the main flow, caused a significant increase in *h* for compound microchannels. As a result, the compound MCHS dissipated more heat from its substrate while maintaining lower wall temperatures.

When pure water is employed as a coolant, the midst zone is cooler than when nanofluids are used, indicating the greatest possible temperature difference of approximately 50°C between the microchannel walls and the coolant, see Figure 9(a). In the case of nanofluids, however, as illustrated in Figure 9(c), the CuO nanofluid has a higher central zone temperature than the others, as well as exhibiting a higher temperature on the walls. The utilization of passive combined approaches, such as the utilization of various nanofluids within the interrupted microchannels, plays a significant role in improving the heat transfer performance of heat exchangers.

Figure 10 elucidates the impact of different nanofluids and MCHS configurations on the average Nusselt number (Nu_{avg}) over a wide volumetric flow rate range ($20 \leq Q_{in} \leq 100$ *ml/min*). It is quite evident that employing nanofluid as a coolant induces higher heat transfer performance than water; however, this comes at the expense of a higher ΔP_t, see Figure 4. When nanoparticles are included to the base fluid, the nanofluid's viscosity increases, resulting in a comparatively higher pumping power than the base fluid. As can be seen, using nanofluids exhibit greater Nu_{avg} values compared to pure water. Moreover, the numerical results obtained revealed that the material of the suspended nanoparticle has a significant effect on Nu_{avg}. On the other

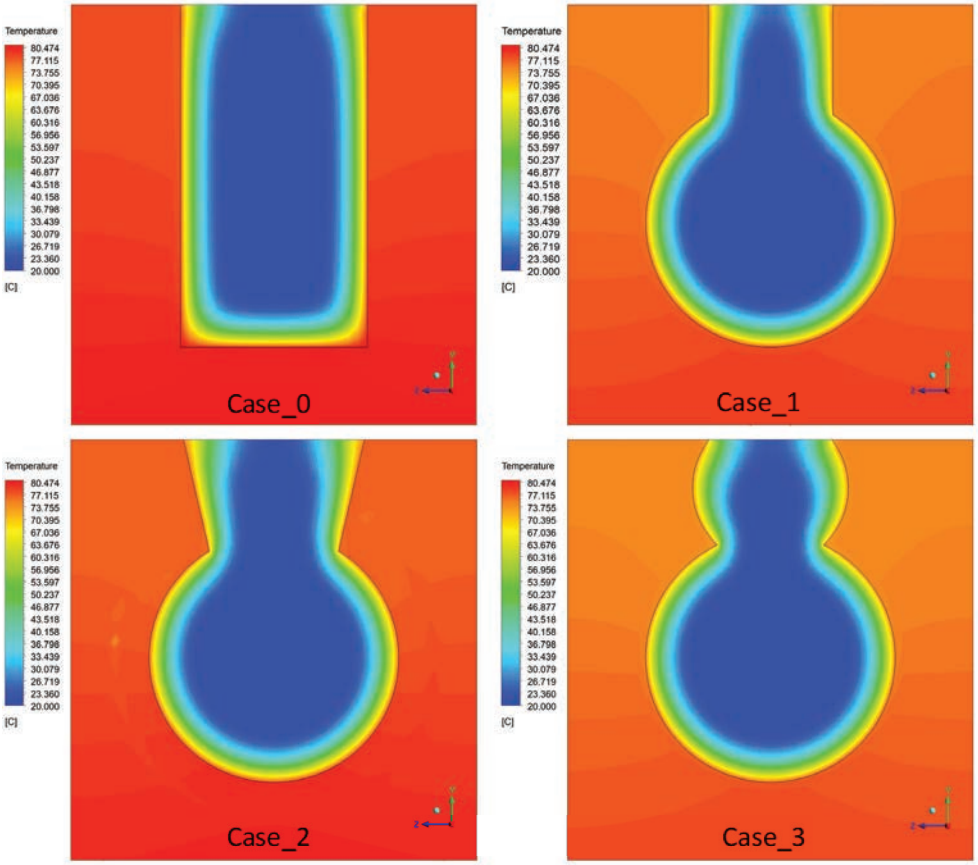
Temperature
80.474
77.115
73.755
70.395
67.036
63.676
60.316
56.956
53.597
50.237
46.877
43.518
40.158
36.798
33.439
30.079
26.719
23.360
20.000
[C]
Case_0
Case_1
Case_2
Case_3

(a)

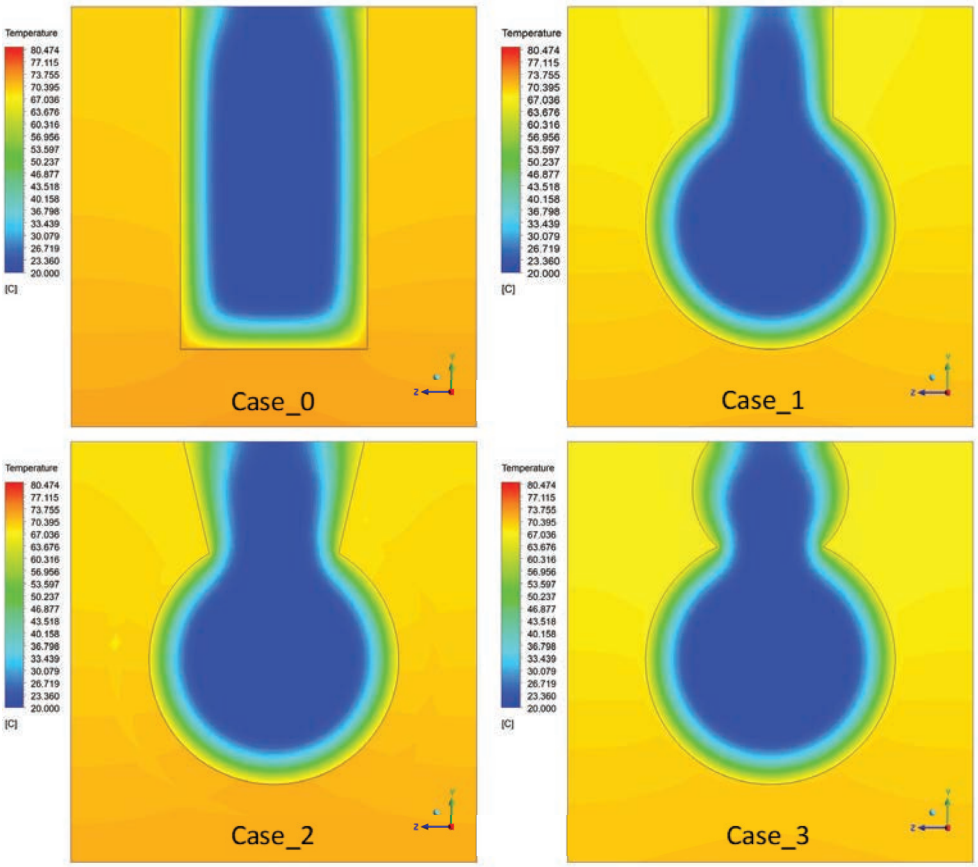
Temperature
80.474
77.115
73.755
70.395
67.036
63.676
60.316
56.956
53.597
50.237
46.877
43.518
40.158
36.798
33.439
30.079
26.719
23.360
20.000
[C]
Case_0
Case_1
Case_2
Case_3

(b)

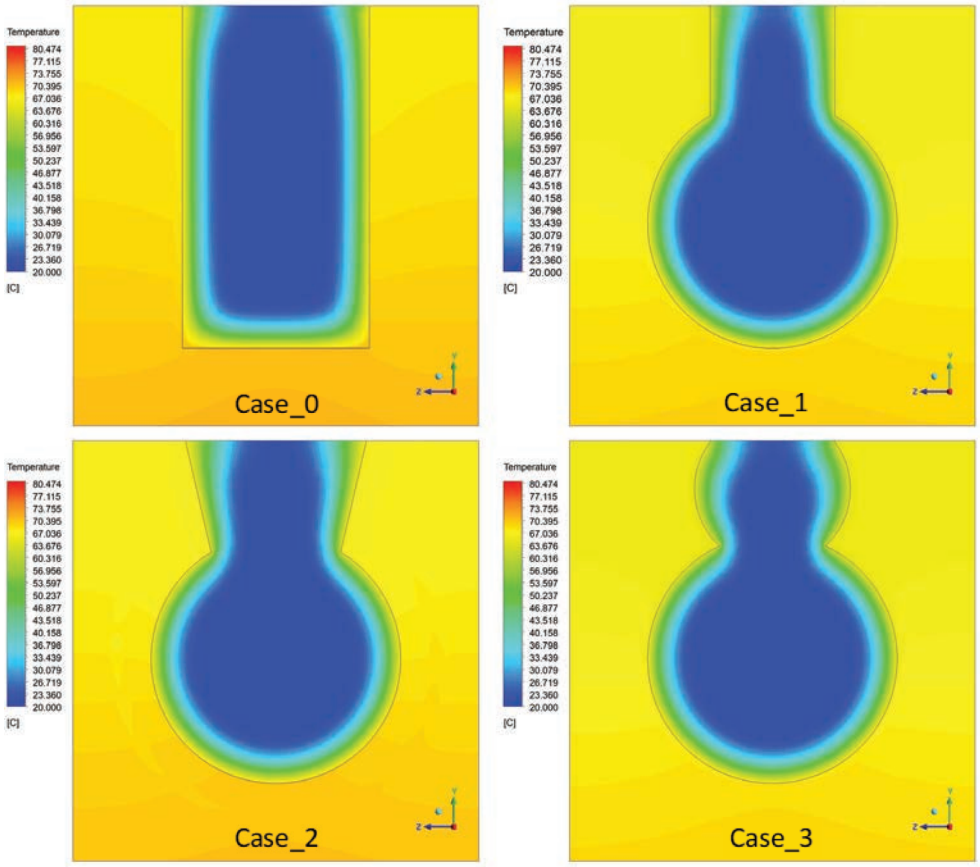

(c)

Figure 9. Comparison of 2D temperature contours for different geometric structures on the y - z plane (x = 20 mm) at the exit region at Q_{in} = 60 ml/min for (a) H_2O, (b) Al_2O_3/H_2O, and (c) CuO/H_2O.

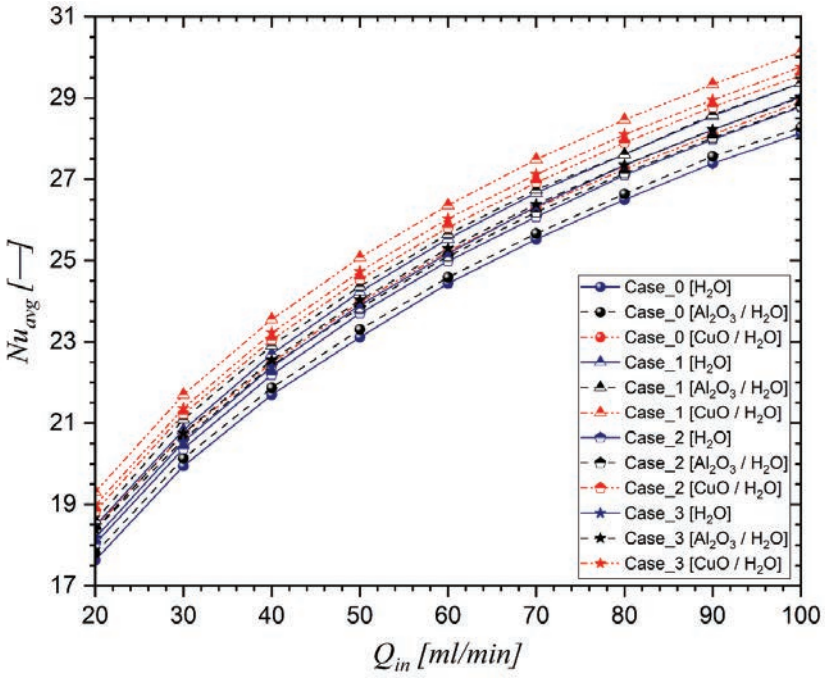

Figure 10. Effect of Q_{in} and nanofluids on the Nu_{avg} for four different MCHS configurations.

hand, the MCHS geometry also has a significant impact in augmenting the Nu_{avg}.

In addition, Figure 10 demonstrates that increasing Q_{in} has a superior effect on enhancing Nu_{avg}. It has been stated that as flow velocity increases, so does turbulent intensity and consequently flow mixing, resulting in improved heat transfer performance. In comparison to low Q_{in}, the Nu_{avg} of higher Q_{in}, presented more improvement by incorporating nanoparticles into the base fluid. As a result of the presence of nanoparticles, the Nu_{avg} of nanofluid is higher than that of the base fluid (water). Furthermore, heat transfer enhancement is associated with collisions between nanoparticles as well as collisions between nanoparticles and the microchannel wall, as a result of which the energy exchange rate rises. Furthermore, the addition of nanoparticles to water increases its thermal conductivity, resulting in a faster heat transfer rate and a higher Nu_{avg}.

To take into account the effect of the thermal conductivity of both nanofluids and water on the heat transfer enhancement, the Nu_{avg} will be considered here for an accurate comparison. For pure water (φ = 0), Figure 10 clearly shows that Case_0 (the traditional MCHS) has the lowest Nu_{avg} than the other MCHS, followed by Case_2 and Case_3, while Case_1 exhibits higher Nu_{avg}. At the highest volumetric flowrate (Q_{in} = 100 *ml/min*), Nu_{avg} in Case_1 (29.37) increased by 4.41% compared to Case_0 (28.13), while Case_3 (29.03) and Case_2 (28.78) enhanced by 3.2% and 2.31%, respectively.

For nanofluids, an increasing trend in Nu_{avg} was observed, with CuO/water nanofluid producing the highest Nu_{avg}. For example, at Q_{in} = 100 *ml/min*, Case_1 with CuO/water nanofluid had the highest Nu_{avg} of 30.13, followed by Case_3 and Case_2 with Nu_{avg} of 29.76 and 29.55, respectively, when CuO/water nanofluid was also used. Case_1 with Al_2O_3/water nanofluid and pure water had the fourth and fifth highest Nu_{avg} values of 29.3696 and 29.3683, respectively, and is nearly identical as can be seen. It is interesting to note that using Case_1 with pure water as a coolant (29.37) outperforms Case_3 with Al_2O_3/water nanofluid (29) and Case_0 with CuO/water nanofluid (28.895). The last values of Nu_{avg} being 28.8 with Case_2 and 28.27 with Case_0 when both used Al_2O_3/water nanofluid.

It was concluded that incorporating nanoparticles into the base fluid resulted in an increased Nusselt number (Nu) as the Q_{in} increased. While the Nu enhancement for the base fluid is not quite profound. However, excessive nanoparticle augmentation causes the dispersed fluid to have a higher viscosity than the base fluid, which reduces heat transfer performance. Additionally, the inclusion of reentrants improved the h by increasing both turbulent intensity and flow mixing.

The effect of fluid type considered in this study on the local average Nusselt number (Nu_{x_avg}) and local average heat flux (q_{x_avg}) in relation to the distance from the microchannel inlet is depicted in Figures 11 and 12, respectively, at Q_{in} = 60 *ml/min*, fluid inlet temperature ($T_{f,in}$) of 20°C and heat flux (q) of 100W/cm². These values are determined at the solid-liquid interface region. From the first glance at the two figures that were mentioned previously, it is worth noting that the values of Nu_{x_avg} and q_{x_avg} decrease along the

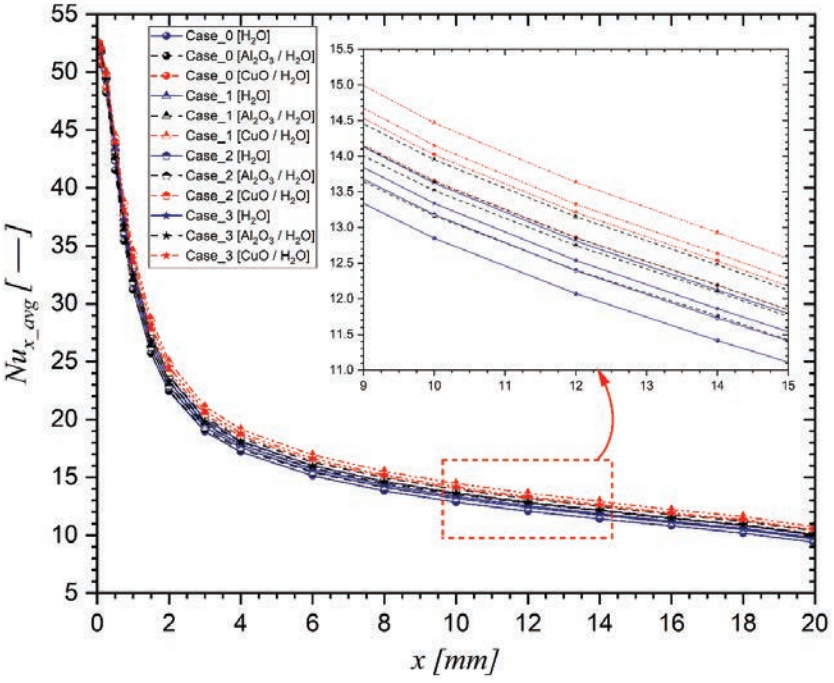

Figure 11. Comparison of the Nu_{x_avg} along the microchannel (x = 0 - 20 *mm*) for different geometric structures and different nanofluids at Q_{in} = 60 *ml/min*.

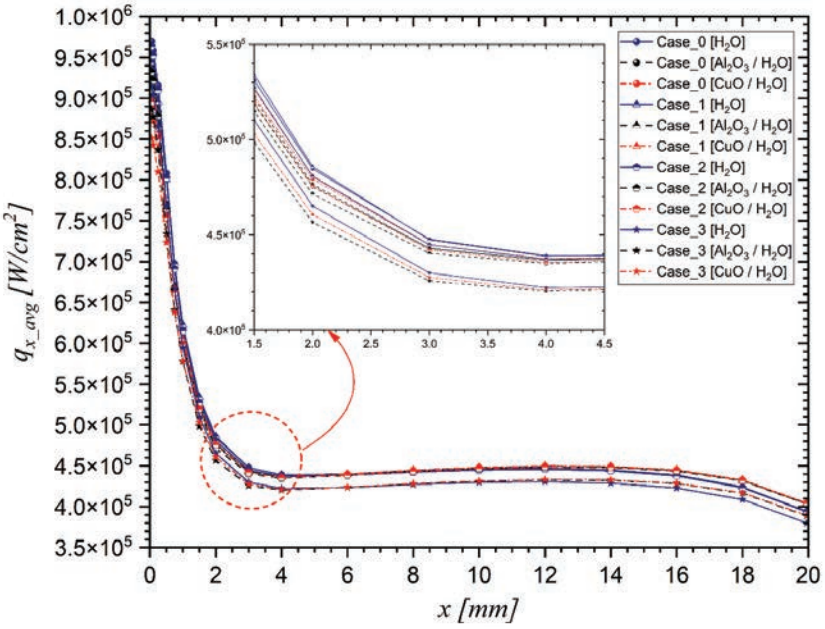

Figure 12. Comparison of the q_{x_avg} along the microchannel (x = 0 - 20 *mm*) for different geometric structures and different nanofluids at Q_{in} = 60 *ml/min*.

microchannel in all cases. The Nu_{x_avg} and q_{x_avg} values are much higher near the microchannel entrance and quickly decrease as one travels down the microchannel. This trend continues even at the microchannel outlet, implying that the length of the thermally developing zone exceeds the length of the microchannel itself even with Case_0 model, this finding is consistent with Ref. [50].

It is clearly that using CuO/water nanofluid exhibits the highest Nu_{x_avg} and q_{x_avg} along the flow direction compared with Al_2O_3 nanofluid. Many factors contributed to nanofluid heat transfer improvement, including particle mixing effects near the wall, thermal conductivity improvement, particle Brownian motion, particle migration, particle shape, and boundary layer thickness reduction.

On the other hand, the figures show lower Nu_{x_avg} and q_{x_avg} distribution with water, indicating lower heat transfer rate. The numerical results also shows that the case_1 model exhibited substantial higher Nu_{x_avg} and q_{x_avg} values than the other designs with all fluid used, as illustrated in Figures 11 and 12.

Thermal Resistance

MCHS's thermal resistance (R_{th}) can be employed to evaluate its cooling performance (see Eq. 13). Three-dimensional numerical simulations were implemented using the ANSYS Fluent CFD code to explore the impact of Al_2O_3/water and CuO/water nanofluids on the R_{th} of the compound MCHS.

As shown in Figure 13, nanofluids can be reduced R_{th} since the maximum wall temperature of nanofluid-cooled MCHS is lower than that of water-cooled MCHS. For instance, Figure 9 shows that water as a coolant has a higher wall temperature than nanofluids. Furthermore, reentrant microchannels exhibit lower R_{th} due to the existence of protrusion, resulting in a greater heat transfer rate and, as a result, a lower wall temperature. The effects of Brownian motion, higher value of k, as well as a larger surface area between the suspended nanoparticles and the base fluid all contribute to this significant decrease in R_{th}.

Performance Analysis

Performance Evaluation Criteria (*PEC*), also known as Performance Factor (*PF*), are computed for all designs by comparing them to the corresponding straight rectangular microchannel (Case_0 model); see Equ. (14). Characteristics of hydrodynamic, thermal, and overall performances are determined by the averaged Nusselt number ratio (E_{Nu}) and the total pressure drop ratio ($E_{\Delta P}$). Figure 14(a-c) show the variation of E_{Nu} and $E_{\Delta P}$ for different geometry structure over a wide volumetric flow rate range ($20 \le Q_{in} \le 100$ *ml/min*). Figure 14(a) illustrates the variation of both E_{Nu} and $E_{\Delta P}$ with different water-based nanofluids and different Q_{in} within the Case_1 model, whereas Figure 14(b and c) depict the variation within Cases 2 and 3, respectively.

As shown in Figure 14, the Case_2 design has the lowest $E_{\Delta P}$ compared to the other designs, while the Case_1 design has the highest. Enlargement of the flow area provided by the trapezoidal slot has contributed to reducing ΔP. The figure also shows that Case_2 with pure water as a coolant has the lowest $E_{\Delta P}$ with $Q_{in} < 40$ *ml/min*, while Case_2 with Al_2O_3/water nanofluid has the lowest $E_{\Delta P}$ within volumetric flow rate of $20 \le Q_{in} \le 40$ *ml/min*, whereas $E_{\Delta P}$ in the

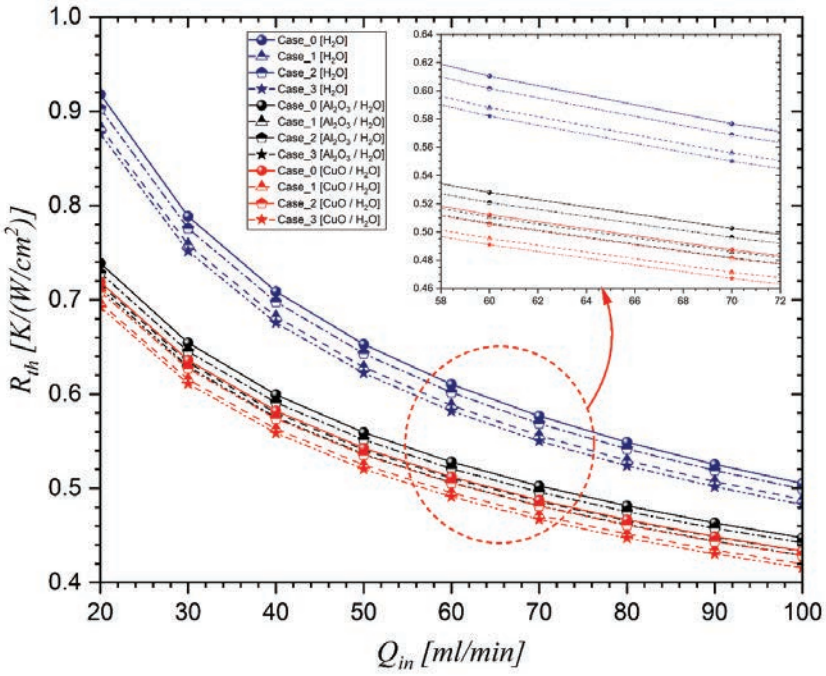

Figure 13. Effect of Q_{in} and different water-base nanofluids on the total thermal resistance for four different MCHS configurations.

case_2 with both Al_2O_3/water and CuO/water nanofluids tend to be identical when $Q_{in} \geq 50$ *ml/min*.

Furthermore, Figure 14 also illustrates how the E_{Nu} varies for different geometry structures and water-based nanofluids that are utilized as indicators for thermal performance criterion (*TPC*). It can be observed that the Case_2 model has lower E_{Nu} due to the stagnation zone effect produced by the upside trapezoidal slot, while the Case_1 design has the highest values of E_{Nu} with all fluids used. For $Q_{in} = 50$ *ml/min*, Case_1 design with pure water shows the great performance to beat other designs ($E_{Nu} = 1.048$). This means that the Case_1 design can outperform others at an intermediate volumetric flow rate ($Q_{in} = 50$ *ml/min*) due to its capability to produce high flow disturbances and vortices, both of which increase flow mixing. It can be concluded that when the Q_{in} is increased, both nanofluids

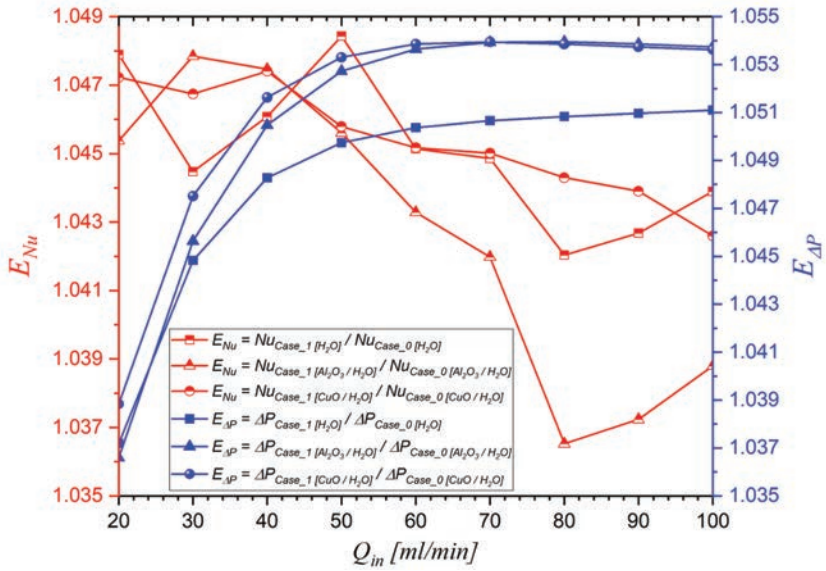

(a)

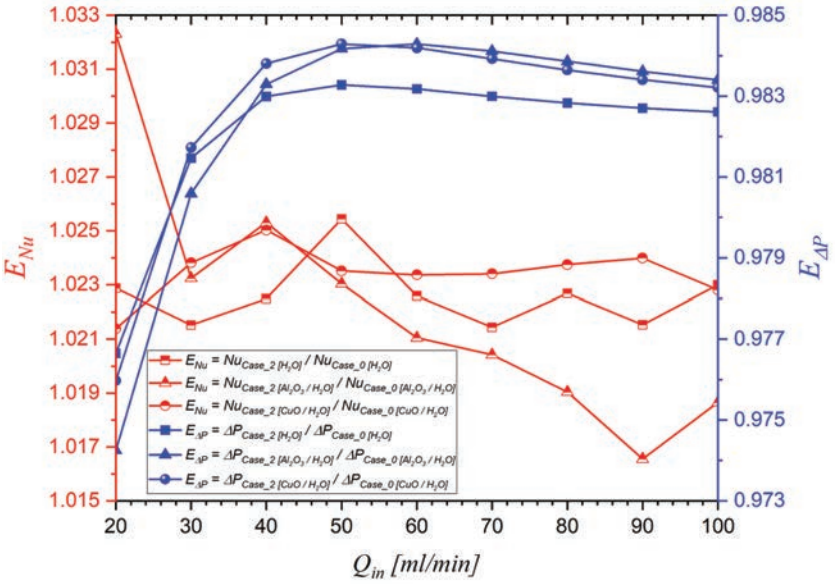

(b)

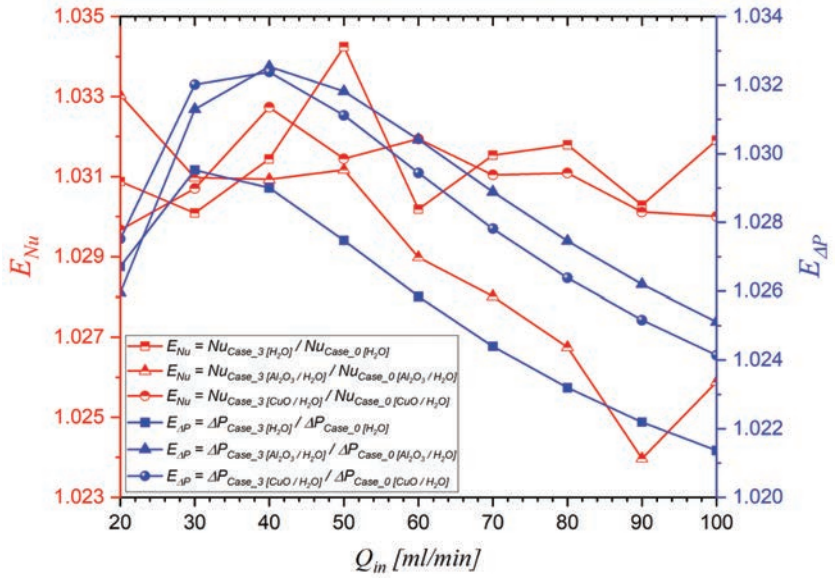

(c)

Figure 14. Variation of Nusselt number ratio and pressure drop ratio with Q_{in} for different geometry structure and different water-base nanofluids for (a) Case_1, (b) Case_2, and (c) Case_3.

and interrupted surfaces deliver superior *TPC* at the cost of a considerable ΔP.

It is revealed that the Nusselt number increment ratios (E_{Nu}) are all in order one from the lowest Q_{in} to the highest Q_{in}. As a result, there are fewer advantages to using nanofluids at high Q_{in} than to using nanofluids at low Q_{in}. When the effects of the ΔP are considered, the significance of this result becomes evident. The presence of nanofluid has the following effects: increased k and nanoparticle collision, both of which are preferred factors for heat transfer augment, as well as an increase in fluid viscosity, which hinders fluid movement and thus heat transfer rate.

In the present study, each MCHS design's overall performance is determined by what is known as a performance factor, *PF*, which can be expressed as the Nusselt number ratio (E_{Nu}) divided by the total pressure drop ratio ($E_{\Delta P}$) to the power of one third. If the *PF* value is greater than one, it indicates that the geometry shape has superior thermal performance and can overcome the disadvantage of the ΔP issue that arises in microchannels. If the value of *PF* is less than one, the condition is reversed.

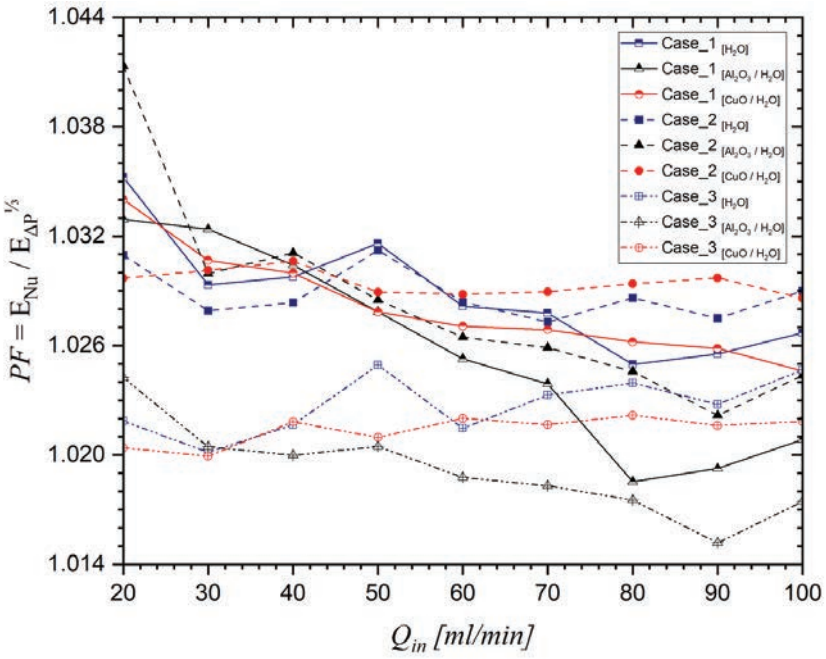

Figure 15. Variation of *PF* with Q_{in} for different geometry structure and different water-base nanofluids.

Figure 15 illustrates the variation of *PF* with Q_{in} for different geometry structure and water-based nanofluids. It can be seen that the Case_2 model outperforms the other designs due to flow interruption by the upside trapezoidal slot. Although Figure 14 shows the E_{Nu} for Case_1 being greater than Case_2, the ΔP that increases with velocity in Case_1 has deteriorated the overall performance of the Case_1 model.

Generally, at Q_{in} < 30 *ml/min*, *PF* of Case_2 with Al_2O_3/water nanofluid is the highest among other MCHS designs. The maximum value of *PF* for Case_2 with Al_2O_3/water nanofluid is found to be 1.041 at Q_{in} = 20 *ml/min*. Unfortunately, as Q_{in} increases, Case_2's performance decreases. The reason behind this phenomenon can be attributed to an increase in both ΔP and wall shear stress as the flow velocity increased and nanoparticles were added. It is worth noting that all of the MCHS models proposed have a *PF* greater than one, indicating that the compound MCHSs can effectively improve heat transfer with only a marginal increase in ΔP, which is attributed to the disruption and reattachment of the flow at reentrant microchannels, which reduces thermal resistance and increases heat transfer rate.

CONCLUSION

This study has demonstrated that utilizing hybrid passive techniques concurrently can augment the MCHS heat transfer efficacy. The first approach uses a novel MCHS design with a bottom circular cavity slotted from the top in various shapes (namely rectangular, trapezoidal, or semicircular reentrant) to form reentrant microchannels, which significantly augments heat transfer by disrupting both the hydrodynamic (δ_{hy}) and thermal boundary layers (δ_{th}), while the second technique uses nanofluids (Al_2O_3/water and CuO/water) with a volume concentration (φ) of 4% to increase the thermal conductivity and viscosity of the base fluid. According to the results obtained, it is observed that as Q_{in} increases, both the pressure drop penalty (ΔP_t) and the average Nusselt number (Nu_{avg}) increase, while the total thermal resistance (R_{th}) decreases. Furthermore, it has been demonstrated that using nanofluid as a coolant can significantly increase the ΔP_t, which can be attributed to an increase in fluid density and viscosity, and thus wall shear stress. However, introducing nanofluid into the microchannel as a coolant can also improve heat transfer.

It is noted that the inclusion of a slot on the top of the curricular cavity can significantly increase the heat transfer coefficient by 3.2–14.6% when compared to the traditional one, owing to the effect of protrusion, which can interrupt the δ_{th}. The newly compound MCHS configurations exerted throttling effects on the fluid flow, causing flow separation. This caused the fluid flow in the main flow within the circular cavity to accelerate, the fluid mixing to intensify, and the continuous development δ_{th} in the cross section to be disrupted. As a result of this, compound microchannels exhibited significantly higher Nu_{avg} and lower wall temperatures. Generally, the compound MCHSs produced a slightly higher pressure drop penalty (ΔP_t) compared with their traditional rectangular counterparts. For pure water (φ = 0), Case_1 has a higher ΔP_t than the other MCHSs, which increased by 5.11% compared to the Case_0 at Q_{in}

= 100 *ml/min*. With nanofluids (φ = 4%) as a coolant, an increasing trend in ΔP_t was observed, with CuO/water nanofluid producing the highest pressure. At Q_{in} = 100 *ml/min*, Case_1 with CuO/water nanofluid had the highest ΔP_t and increased by 45.8% compared to the Case_0 utilizing water as a coolant. The highest value of performance factor (*PF*) is obtained from a Case_2 with Al_2O_3/water nanofluid at lower flow rate (Q_{in} = 20 *ml/min*).

The study's findings are expected to assist designers in developing more efficient MCHS systems. Future studies on electronic device cooling can investigate the effect of various cooling channel geometry, nanofluid as a cooling medium, nanofluid volume fraction, and nanoparticle size on heat transfer enhancement.

ACKNOWLEDGEMENTS

The authors would like to thank the University of Mosul for the facilities used in this study.

AUTHORSHIP CONTRIBUTIONS

Authors equally contributed to this work.

DATA AVAILABILITY STATEMENT

The authors confirm that the data that supports the findings of this study are available within the article. Raw data that support the finding of this study are available from the corresponding author, upon reasonable request.

CONFLICT OF INTEREST

The authors declared no potential conflicts of interest with respect to the research, authorship, and/or publication of this article.

ETHICS

There are no ethical issues with the publication of this manuscript.

NOMENCLATURE

A_{ch}	Microchannel cross-sectional area [m^2]
A_{con}	Convective heat transfer area [m^2]
A_{ht}	MCHS bottom heated area [m^2]
C_p	Specific heat capacity [J/kg.K]
D_h	Hydraulic diameter [m]
d_{np}	Nanoparticle diameter [m]
h	Convective heat transfer coefficient [W/m^2.K]
H	Heat sink height [m]
H_b	Substrate thickness [m]
H_{ch}	Microchannel height [m]
k	Thermal conductivity [W/m.K]
K_B	Boltzmann's constant
L	Heat sink length [m]
L_{ch}	Microchannel length [m]
M	Molecular weight
N	Avogadro number
N_{ch}	Number of microchannel
Nu	Nusselt number
P_{ch}	Wetted perimeter [m]
PF	Performance factor
Pr	Prandtl number
ΔP	Total pressure drop [Pa]
Q	Sensible heat gain [W]
Q_{in}	Volumetric flow rate [m^3/sec]
q	Heat flux [W/cm^2]
Re	Reynolds number
R_{th}	Total thermal resistance [K/W]
T_f	Fluid temperature [°C]
$T_{f,avg}$	Fluid bulk temperature [°C]
T_{fr}	Freezing point temperature of the water [°C]
$T_{w,avg}$	Average channel base temperature [°C]
u_B	Nanoparticle mean Brownian velocity [m/s]
u_{in}	Uniform inlet velocity [m/s]
V	Total volume of the solution [m^3]
W_{ch}	Microchannel width [m]
W	Heat sink width [m]

Greek symbols

ρ	Density [kg/m^3]
μ	Dynamic viscosity [kg/m s]
φ	Volume fraction [%]
π	Pi (= 3.14)

Subscripts

avg	Average
bf	Base fluid (Water)
f	Fluid
in	Inlet
max	Maximum
nf	Nanofluid
np	Nanoparticle
out	Outlet
s	Solid
Γ	Interface between the fluid and solid
x	Streamwise coordinate
y	Normal coordinate
z	Spanwise coordinate

REFERENCES

[1] Zhou G, Zhou J, Huai X, Zhou F, Jiang Y. A two-phase liquid immersion cooling strategy utilizing vapor chamber heat spreader for data center servers. Appl Therm Eng 2022;210:118289. [CrossRef]

[2] Tuckerman DB, Pease RFW. High-performance heat sinking for VLSI. IEEE Electron Device Lett 1981;2:126−129. [CrossRef]

[3] Sidik NAC, Muhamad MNAW, Japar WMAA, Rasid ZA. An overview of passive techniques for heat transfer augmentation in microchannel heat sink. Int Commun Heat Mass Transf 2017;88:74−83. [CrossRef]

[4] Dai Z, Fletcher DF, Haynes BS. Impact of tortuous geometry on laminar flow heat transfer in microchannels. Int J Heat Mass Transf 2015;83:382–398. [CrossRef]
[5] Parlak Z. Optimal design of wavy microchannel and comparison of heat transfer characteristics with zigzag and straight geometries. Heat Mass Transf 2018;54:3317–3328. [CrossRef]
[6] Lin L, Zhao J, Lu G, Wang XD, Yan WM. Heat transfer enhancement in microchannel heat sink by wavy channel with changing wavelength/amplitude. Int J Therm Sci 2017;118:423–434. [CrossRef]
[7] Al-Neama AF, Kapur N, Summers J, Thompson HM. An experimental and numerical investigation of the use of liquid flow in serpentine microchannels for microelectronics cooling. Appl Therm Eng 2017;116:709–723. [CrossRef]
[8] Al-Neama AF, Kapur N, Summers J, Thompson HM. Thermal management of GaN HEMT devices using serpentine minichannel heat sinks. Appl Therm Eng 2018;140:622–636. [CrossRef]
[9] Al-Neama AFM. Serpentine minichannel liquid-cooled heat sinks for electronics cooling applications [dissertation]. University of Leeds, School of Mechanical Engineering; 2018.
[10] Al-Neama AF, Khatir Z, Kapur N, Summers J, Thompson HM. An experimental and numerical investigation of chevron fin structures in serpentine minichannel heat sinks. Int J Heat Mass Transf 2018;120:1213–1228. [CrossRef]
[11] Kilic M, Sahin M, Iqbal M, Demircan T, Kilinc Z, Ullah A. Numerical investigation of cooling an industrial roller by using swirling jets. El-Cezeri J Sci Eng 2023;10:147–159. [CrossRef]
[12] Wang W, Li Y, Zhang Y, Li B, Sundén B. Analysis of laminar flow and heat transfer in an interrupted microchannel heat sink with different shaped ribs. J Therm Anal Calorim 2020;140:1259–1266. [CrossRef]
[13] Deng D, Wan W, Tang Y, Shao H, Huang Y. Experimental and numerical study of thermal enhancement in reentrant copper microchannels. Int J Heat Mass Transf 2015;91:656–670. [CrossRef]
[14] Hou T, Chen Y. Pressure drop and heat transfer performance of microchannel heat exchanger with circular reentrant cavities and ribs. J Heat Transf 2020;142:042502. [CrossRef]
[15] Chen L, Deng D, Ma Q, Yao Y, Xu X. Performance evaluation of high concentration photovoltaic cells cooled by microchannels heat sink with serpentine reentrant microchannels. Appl Energy 2022;309:118478. [CrossRef]
[16] Liu L, Cao Z, Xu C, Zhang L, Sun T. Investigation of fluid flow and heat transfer characteristics in a microchannel heat sink with double-layered staggered cavities. Int J Heat Mass Transf 2022;187:122535. [CrossRef]
[17] Wang RJ, Wang JW, Lijin BQ, Zhu ZF. Parameterization investigation on the microchannel heat sink with slant rectangular ribs by numerical simulation. Appl Therm Eng 2018;133:428–438. [CrossRef]
[18] Chai L, Wang L, Bai X. Thermohydraulic performance of microchannel heat sinks with triangular ribs on sidewalls-Part 1: Local fluid flow and heat transfer characteristics. Int J Heat Mass Transf 2018;127:1124–1137. [CrossRef]
[19] Chai L, Wang L, Bai X. Thermohydraulic performance of microchannel heat sinks with triangular ribs on sidewalls-Part 2: Average fluid flow and heat transfer characteristics. Int J Heat Mass Transf 2019;128:634–648. [CrossRef]
[20] Wang G, Qian N, Ding G. Heat transfer enhancement in microchannel heat sink with bidirectional rib. Int J Heat Mass Transf 2019;136:597–609. [CrossRef]
[21] Ali S, Ahmad F, Akhtar K, Habib N, Aamir M, Giasin K, Vafadar A, Pimenov DY. Numerical investigation of microchannel heat sink with trefoil shape ribs. Energies 2021;14:6764. [CrossRef]
[22] Chen H, Chen C, Zhou Y, Yang C, Song G, Hou F, Jiao B, Liu R. Evaluation and optimization of a cross-rib micro-channel heat sink. Micromachines 2022;13:132. [CrossRef]
[23] Datta A, Sharma V, Sanyal D, Das P. A conjugate heat transfer analysis of performance for rectangular microchannel with trapezoidal cavities and ribs. Int J Therm Sci 2019;138:425–446. [CrossRef]
[24] Zhu Q, Chang K, Chen J, Zhang X, Xia H, Zhang H, Wang H, Li H, Jin Y. Characteristics of heat transfer and fluid flow in microchannel heat sinks with rectangular grooves and different shaped ribs. Alex Eng J 2020;59:4593–4609. [CrossRef]
[25] Hong F, Cheng P. Three dimensional numerical analyses and optimization of offset strip-fin microchannel heat sinks. Int Commun Heat Mass Transf 2009;36:651–656. [CrossRef]
[26] Jia Y, Xia G, Li Y, Ma D, Cai B. Heat transfer and fluid flow characteristics of combined microchannel with cone-shaped micro pin fins. Int Commun Heat Mass Transf 2018;92:78–89. [CrossRef]
[27] Bhandari P, Prajapati YK. Thermal performance of open microchannel heat sink with variable pin fin height. Int J Therm Sci 2021;159:106609. [CrossRef]
[28] Shiko SS, Al-Neama AF. Numerical investigation of the hydrothermal characteristics of water flow in compound microchannel heat sinks. Int J Adv Res Eng Innov 2023;5:1–15.
[29] Choi SUS, Eastman JA. Enhancing thermal conductivity of fluids with nanoparticles. ASME Int Mech Eng Congr Expo 1995;12–17.
[30] Eastman JA, Choi SUS, Li S, Thompson LJ, Lee S. Enhanced thermal conductivity through the

development of nanofluids. Proceedings of the Symposium on Nanophase and Nanocomposite Materials II, Mater Res Soc, Boston 1997;457:3–11. [CrossRef]

[31] Gupta M, Singh V, Kumar R, Said Z. A review on thermophysical properties of nanofluids and heat transfer applications. Renew Sustain Energy Rev 2017;74:638–670. [CrossRef]

[32] Sajid MU, Ali HM, Sufyan A, Rashid D, Zahid SU, Rehman WU. Experimental investigation of TiO_2–water nanofluid flow and heat transfer inside wavy mini-channel heat sinks. J Therm Anal Calorim 2019;137:1279–1294. [CrossRef]

[33] Khoshvaght-Aliabadi M, Hassani SM, Mazloumi SH. Enhancement of laminar forced convection cooling in wavy heat sink with rectangular ribs and Al_2O_3/water nanofluids. Exp Therm Fluid Sci 2017;89:199–210. [CrossRef]

[34] Naranjani B, Roohi E, Ebrahimi A. Thermal and hydraulic performance analysis of a heat sink with corrugated channels and nanofluids. J Therm Anal Calorim 2021;146:2549–2560. [CrossRef]

[35] Saadoon ZH, Ali FH, Hamzah HK, Abed AM, Hatami M. Improving the performance of mini-channel heat sink by using wavy channel and different types of nanofluids. Sci Rep 2022;12:9402. [CrossRef]

[36] Ullah A, Kilic M, Habib G, Sahin M, Khalid RZ, Sanaullah K. Reliable prediction of thermophysical properties of nanofluids for enhanced heat transfer in process industry: A perspective on bridging the gap between experiments, CFD and machine learning. J Therm Anal Calorim 2023;148:5859–5881. [CrossRef]

[37] Kokate YD, Sonawane SB. Investigation of particle size effect on thermal conductivity enhancement of distilled water-Al_2O_3 nanofluids. Fluid Mech Res Int J 2019;3:55–59. [CrossRef]

[38] Chai L, Xia GD, Wang HS. Laminar flow and heat transfer characteristics of interrupted microchannel heat sink with ribs in the transverse microchambers. Int J Therm Sci 2016;110:1–11. [CrossRef]

[39] McCutcheon SC, Martin JL, Barnwell TO. Handbook of Hydrology. New York: McGraw-Hill; 1993.

[40] Sherman FS. Viscous Flow. New York: McGraw-Hill; 1990.

[41] Bergman TL, Lavine AS, Incropera FP, Dewitt DP. Fundamentals of Heat and Mass Transfer. 7th ed. New York: John Willey & Sons; 2011.

[42] Mahdi RA, Mohammed HA, Munisamy KM, Saeid NH. Review of convection heat transfer and fluid flow in porous media with nanofluid. Renew Sustain Energy Rev 2015;41:715–734. [CrossRef]

[43] Pack BC, Cho YI. Hydrodynamic and heat transfer study of dispersed fluids with submicron metallic oxide particles. Exp Heat Transf 1998;11:151–170. [CrossRef]

[44] Khanafar K, Vafai K, Lightstone M. Buoyancy-driven heat transfer enhancement in a two-dimensional enclosure utilizing nanofluids. Int J Heat Mass Transf 2003;46:3639–3653. [CrossRef]

[45] Buongiorno J. Convective transport in nanofluids. J Heat Transf 2005;128:240–250. [CrossRef]

[46] Corcione M. Empirical correlating equations for predicting the effective thermal conductivity and dynamic viscosity of nanofluids. Energy Convers Manag 2011;52:789–793. [CrossRef]

[47] Keblinski P, Phillpot SR, Choi SUS, Eastman JA. Mechanisms of heat flow in suspensions of nano-sized particles (nanofluids). Int J Heat Mass Transf 2002;45:855–863. [CrossRef]

[48] Sasmito AP, Kurnia JC, Mujumdar AS. Numerical evaluation of laminar heat transfer enhancement in nanofluid flow in coiled square tubes. Nanoscale Res Lett 2011;6:376. [CrossRef]

[49] Kawano K, Minakami K, Iwasaki H, Ishizuka M. Microchannel heat exchanger for cooling electrical equipment. Appl Heat Transf Equip Syst Educ 1998;3:173–180. [CrossRef]

[50] Qu W, Mudawar I. Analysis of three-dimensional heat transfer in microchannel heat sinks. Int J Heat Mass Transf 2002;45:3973–3985. [CrossRef]